Laminin alpha 5 - induced mechanical homeostasis modulates retinal epithelium functionality

Aleksandra N. Kozyrina* [1, 2], Teodora Piskova* [1, 2], Iris Doolaar [3], Taspia Prapty [1, 2], Francesca Semeraro [1, 2], Lok Sze Yam[1, 2], Tamás Haraszti [3], Maxime Hubert [4, 5], Ana-Sunčana Smith [4, 5] and Jacopo Di Russo[1, 2, 3]

* equal contribution

1. Interdisciplinary Centre for Clinical Research, RWTH Aachen University, Pauwelstrasse 30, 52074 Aachen, Germany.
2. Institute of Molecular and Cellular Anatomy, RWTH Aachen University, Wendlingweg 2, 52074 Aachen, Germany.
3. DWI – Leibniz-Institute for Interactive Materials, Forckenbeckstrasse 50, 52074 Aachen, Germany.
4. PULS Group, Department of Physics and Interdisciplinary Center for Nanostructured Films, Friedrich-Alexander University of Erlangen-Nürnberg, 91058 Erlangen, Germany.
5. Group for Computational Life Sciences, Division of Physical Chemistry, Rudjer Bošković Institute,10000 Zagreb, Croatia.

Correspondence:

Jacopo Di Russo

jdirusso@ukaachen.de

ABSTRACT

Epithelial cells are highly interconnected, whereby they acquire mesoscale mechanical properties to accomplish specific tissue functions. In homeostasis, these mechanical features can be summarised as mechanical homeostasis, regulated by the balance of intercellular tension and extracellular matrix adhesion forces. In the outer retina, the significance of these forces in defining its mechanical homeostasis and vision remains poorly understood. The retinal pigmented epithelium (RPE) is located at the base of the retina and supports vision by ensuring the light sensitivity and lifespan of photoreceptor cells. Due to different photoreceptor densities, this functional demand on the RPE varies from the most illuminated macula to the less illuminated retinal periphery and corresponds to a significant difference in monolayer organisation. In this work, we hypothesised that extracellular matrix cues define the relation between RPE organisation, mechanical status and functional demand. We found that the density of basement membrane laminin alpha 5 modulates RPE contractility levels which directly control the epithelium efficiency in phagocyting photoreceptor outer segments. *In vivo*, laminin alpha 5 density gradient follows retinal functional demand, thus supporting the physiological role of laminin alpha 5 in controlling RPE mechanical homeostasis. ECM-defined mechanical status of the RPE provides a novel parameter to consider for visual function and opens new paths of investigation for sight-threatening diseases such as high myopia and age-related macular degeneration.

The mechanical properties of any tissue define its function and state (Anlaş & Nelson, 2018; Ayad *et al*, 2019). In a homeostatic state, these mechanical features are maintained in a preferred range for optimal activity, also known as tissue mechanical homeostasis (Eichinger *et al*, 2021). One of the main players in defining the mechanical homeostasis of tissues is its extracellular matrix (ECM) composition (Humphrey *et al*, 2014; Kozyrina *et al*, 2020).

The retinal pigmented epithelium (RPE) is a postmitotic cell monolayer located at the base of the light-detecting neural retina. In the developing eye, the RPE organises the retina (Raymond & Jackson, 1995; German *et al*, 2008), while in the adult, it plays a key role in the visual cycle (Bok, 1993; Strauss, 2005). One of the main activities of each RPE cell is the daily phagocytosis of shed photoreceptors fragments, therefore mediating the constant renewal of light-sensitive outer segments and ensuring photoreceptor lifespan and light sensitivity (Lakkaraju *et al*, 2020; Young & Bok, 1969; Wald & Brown, 1956). The number of photoreceptor outer segments (POS) per RPE cells is not constant within the eye, with an average of 30-25 POS per RPE cell in the central and macular area and decreasing towards the periphery (Volland *et al*, 2015), indicating a gradient of functional demand. Cells of the RPE are polygonal in shape and tightly adhere to each other, arranged as a honeycomb-like structure in the centre, and gradually shifts to a more elongated and less organised structure towards the retinal periphery (Bhatia *et al*, 2016; Kim *et al*, 2021) suggesting a change in its mechanical status. The RPE is tightly bound to its underlying basement membrane, part of the thicker Bruch's membrane. The Bruch's membrane thickness and content of fibrillar collagens and elastin are known to vary from the centre to the periphery (Chong *et al*, 2005; Newsome *et al*, 1987), but to date is still unclear how this affects the overall mechanical properties of the ECM and, more importantly, if this variability is also present for RPE basement membrane components. Furthermore, whether any relation exists between ECM heterogeneity and RPE mechanical homeostasis is still an open question.

Here we hypothesise that the spatial variation of Bruch's membrane cues controls the RPE mechanical homeostasis and the region-dependent functional demand. The characterisation of Bruch's membrane composition in mice revealed a relative density reduction of specific basement membrane laminins towards the periphery. Decreased density of laminin 511 also reduces POS phagocytic efficiency in stem cell-derived RPE monolayers obtained on polyacrylamide soft hydrogels. This is associated with different RPE mechanical status, particularly with increased RPE contractility, quantified by traction force and monolayer stress microscopy. Finally, using different hydrogels stiffnesses, coatings and modulating actomyosin activity with drugs, we show that the POS phagocytosis efficiency results from RPE contractility levels. These findings underline for the first time the importance of mechanical homeostasis in RPE, and in general, the outer retina. The significance of RPE mechanical status for

visual function in adults opens the question of its role in ageing and sight-threatening diseases such as (high) myopia and age-related macular degeneration.

RESULTS

The Bruch's membrane presents biochemical heterogeneity correlating with different RPE mechanical homeostasis

To understand the possible relation of ECM biochemical and mechanical cues with RPE mechanobiology, we characterised the Bruch's membrane of adult BALB/C mice (25-30 weeks) (Fig 1). Bruch's membrane, retinal complexity and function have been described in relation to the sightline or visual axis (Volland *et al*, 2015). In mice and humans, the central part (macula in humans) has the highest density of photoreceptor cells and the highest photoreceptor to RPE ratio, both decreasing with the radial distance from the optic nerve (Volland *et al*, 2015). Hence, we identified three regions with respect to the radial distance from the optic nerve: centre (300-1200 μm), mid-periphery (1200-2000 μm) and far-periphery (2000-3000 μm) (Fig. 1 A). As reported, we also observed that RPE cell arrangement and organisation along the radial distance changes significantly (Fig. 1 A) in agreement with previous reports (Bhatia *et al*, 2016; Kim *et al*, 2021). From a classic honeycomb arrangement in the centre, the RPE gradually changes to a monolayer made by more elongated cells in the far-periphery (Fig. 1 A; Sup fig. 1 A, D) (Bhatia *et al*, 2016; Kim *et al*, 2021).

The topology and morphology of an epithelial monolayer define its mechanical properties (Hannezo *et al*, 2014; Alt *et al*, 2017; Kaliman *et al*, 2021). Hence, we performed morphometric characterisation of the RPE cells in the different regions of the retina (Fig.1 B - D, sup. fig. 1 A - H). RPE cells have the largest area and perimeter in the central region (A = 469 μm^2; P = 84 μm), whereas they assume smaller size in mid-periphery (A = 349 μm^2; P = 74 μm) and far-periphery (A = 343 μm^2; P = 75 μm) (Sup. fig.1 F, G). Next, to better quantify the mechanical consequences of the differential cell arrangement, for each cell we calculated the shape factor, which is defined as the cell perimeter P divided by the square root of the corresponding cell area A. This density-independent shape factor has been theorised to describe epithelial rigidity based on the ratio of cortical tension vs cell-cell adhesion energy with lower values where the first element is prominent (Bi *et al*, 2015). Our data show an average value of 3.8 in the retinal central region, which gradually increases till reaching values over 4.0 at the far-periphery, suggesting a gradual increase of intercellular tension concurrently with the decreasing RPE functional demand (Fig. 1 B, C, sup. fig. 1 E) (Volland *et al*, 2015). Finally, we noticed the presence of two distinct cell populations at the centre and mid-periphery, which are visible when cell area and cell perimeter distributions are normalised and compared (Fig. 1 D, sup. fig. 1 H). Hence, we compared the topological relations of the retinal regions by plotting the rescaled cell areas and

perimeters in relation to their number of neighbours (respectively Lewis' law (Lewis, 1931, 1928; Chiu, 1995; Kim *et al*, 2014) and Desh's law (Rivier, 2006)) (Fig. 1 E, sup. fig. 1 I, J). Both comparisons show different curve behaviour in the different retinal regions, especially evident between centre and far periphery.

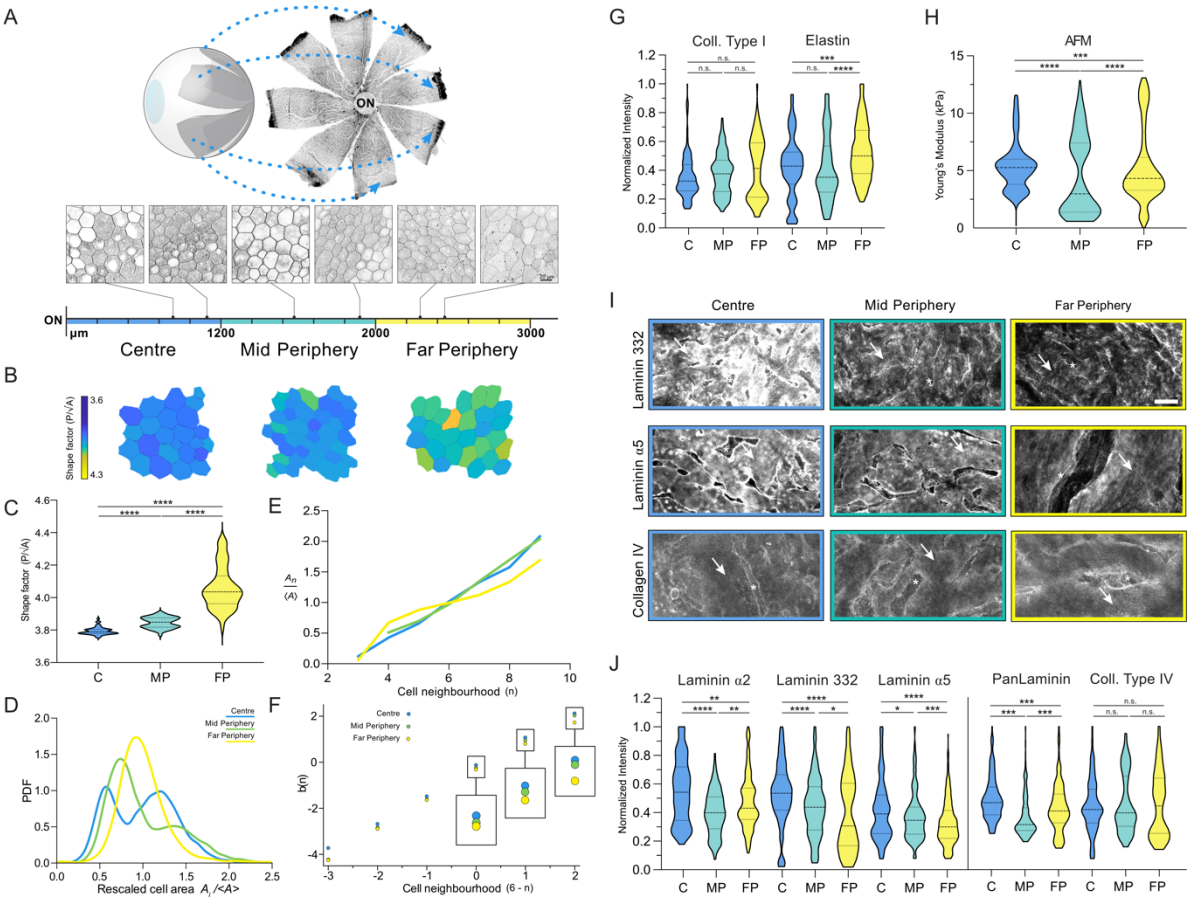

Figure 1: Spatial heterogeneity of murine retinal pigment epithelium topology and Bruch's membrane composition. *(**A**) Murine retina flat mount indicating the regions used for analyses and representative F-actin staining of RPE. The regions were defined by the distance from the optic nerve head: centre (300 - 1200 µm), mid-periphery (1200 – 2000 µm) and periphery (2000 – 3000 µm). (**B**) Representative cell shape index maps for the three regions. The shape index is identified as the perimeter divided by the square root of the area for every cell. (**C**) Violin plot of mean tissue shape factors from the different regions of the eye analysed from 7 mice. (**D**) The probability density function (PDF) of the rescaled cell areas defined by $A_i/\langle A\rangle$, A_i being the individual cell area and $\langle A\rangle$ being the average cell area within a given image. More than 5500 cells were analysed from 3 mice. (**E**) Lewis' law representing the relationship between rescaled cell area and neighbourhood varying for three different regions from 3 mice. (**F**) Aboav-Weaire's laws showing the variation of the topological parameter b(n) depending on the number of neighbours for each cell between different retinal regions from 3 mice. (**G**) Violin plots of mean fluorescence intensity of interstitial matrix components of the Bruch's membrane. Data were collected from 3 mice and normalized to the highest intensity per mouse. (**H**) Violin plots of the regional Young's modulus of the Bruch's membrane from 5 mice. (**I**) Representative immunofluorescent images of the Bruch's membrane stained for laminin-332, laminin α5 and collagen type IV. Arrows and stars indicate RPE basement membrane surface and preparation artefacts respectively. Scale bar 20 µm. (**J**) Violin plots of mean fluorescence intensity of basement membrane components: laminin α2, laminin 332, laminin α5, pan-laminin, and collagen type IV. Each region contains the quantification of at least 7 sectors from a minimum of 3 to 6 mice. The data were statistically tested with Mann-Whitney test: *p < 0.05; ** p < 0.01; *** p < 0.001; **** p < 0.0001; n.s. = not significant.*

73 Furthermore, we correlated the number of neighbours *(n)* of each cell and the average number of
74 neighbours *m(n)* of any adjacent cells to the first with *n* sides (Aboav-Weaire's laws) (Fig. 1 E, F) (Aboav,
75 1980, 1970; Weaire, 1974). This relation describes the topology of epithelial monolayers via the
76 topological parameter *b(n)* (see method section). The measurements of the different regions show
77 linear relationship, as in any functional epithelium (Aboav, 1980, 1970; Weaire, 1974; Kaliman *et al*,
78 2021). Nevertheless, a shift is visible between curves, thus suggesting a topological variation of RPE
79 from the centre to the far-periphery (Fig. 1 F, sup. fig. I). Altogether, the extensive image-based
80 morphometric and topological analyses (of more than 5500 cells) strongly support the existence of
81 different mechanical status of the monolayer from the retinal central region to the far periphery.
82 Next, we were curious to know if the quantified mechanical gradient of RPE finds a correlation with the
83 distribution of mechanical and biochemical cues within the Bruch's membrane. In the epithelial ECM,
84 mechanical cues are mostly determined by the interstitial matrix composition and crosslinking (Kozyrina
85 *et al*, 2020). Therefore, we use confocal microscopy and immunofluorescence staining to quantify the
86 amount of collagen type I and elastin present only at Bruch's membrane level. The average intensity
87 quantification of the retina's centre, mid-periphery, and far-periphery regions are comparable with the
88 data reported in the literature (Chong *et al*, 2005; Newsome *et al*, 1987) (Fig. 1 G). Next, we quantified
89 the Young's modulus of the Bruch's membrane in the different regions using an atomic force
90 microscope (AFM) and indenting the decellularised ECM by 200 nm. The quantification resulted in a
91 highly variable distribution of the data, with the centre having the most frequent (mode) stiffness of
92 5.5 kPa, the mid-periphery of 1.5 kPa and the far-periphery of 4 kPa (Fig. 1 H). This biphasic trend of
93 the stiffness suggests that ECM mechanical cues may not be the main player in regulating RPE
94 mechanical homeostasis in relation to the functional demand.
95 The basement membrane provides biochemical cues to epithelia regulating its homeostasis with a key
96 role of the different laminin isoforms (Kozyrina *et al*, 2020). Thus, we characterised the composition
97 and relative amount of the main basement membrane components in the Bruch's membrane, namely
98 laminins and collagen type IV (Fig. 1 I, J). Interestingly, we detected a significant change in laminin
99 isoforms amount along the visual axis but not in collagen type IV (Fig. 1 I, J), supporting the idea of
100 the importance of laminins in the differential biochemical signalling to the RPE. Among the laminin
101 isoforms detected in the Bruch's membrane, we noticed a biphasic trend of laminin α2 containing
102 isoforms, with higher (fluorescence) intensity in the centre and far-periphery and lower in the mid-
103 periphery. On the contrary, laminin 332 and laminin α5 containing isoforms were found to have the
104 highest (fluorescence) intensity in the centre and to gradually decrease towards the periphery
105 (Fig. 1 I, J). No laminin α1– or α4-containing isoforms were detected.

106 Altogether, the characterisation of the murine retina suggests a possible relationship between the
107 relative density of Bruch's membrane's laminins and RPE regional mechanical status.
108
109 **Laminin density influences RPE phagocytic activity of photoreceptor outer segments.**
110 To dissect the hypothesis of a direct relation between biochemical cues from Bruch's membrane and
111 RPE mechanobiology, we established a bottom-up approach to examine the role of the specific laminin
112 isoforms and their density gradient. Human induced pluripotent stem cell-derived RPE (hiPSC-RPE)
113 cells have already been successfully employed to model mature RPE and to study their functionality
114 (Song *et al*, 2023; Müller *et al*, 2018). Thus, we obtained RPE monolayers on polyacrylamide (PAA)
115 hydrogels with 4 kPa Young's modulus to best mimic Bruch's membrane stiffness. The gels were
116 functionalised according to Przybyla et al. (Przybyla *et al*, 2016) with specific concentrations of laminin,
117 thus controlling the protein density at the surface in a reproducible manner (see materials and
118 methods). The advantage of PAA gel as a culture substrate is the polymer's protein-repellent nature
119 (Funaki & Janmey, 2017), allowing control over the biochemical cues originating from the coating and
120 a defined stiffness (gel's Youngs's modulus). Due to this reductionist approach, certain coating
121 conditions were not permissive to obtain mature and intact RPE monolayers, such as laminin 511 and
122 collagen type IV alone or laminin 211 also in combination with collagen type IV (Sup. fig. 2 A - C).
123 Nevertheless, hiPSC-RPE cells adhere and form a mature monolayer when seeded on PAA gels coated
124 with different concentrations of laminin 332 and laminin 511, both in combination with collagen type
125 IV. After a week of culture, hiPSC-RPE cells reach a low proliferative state and form a thick polarised
126 monolayer (~10 - 15 µm), presenting apical microvilli as shown by ezrin staining and scanning electron
127 microscopy (Fig. 2 A - C). Furthermore, the staining for fibronectin confirmed the absence of aberrant
128 deposition of ECM proteins by the cells while cultured (Sup. fig. 2 D).
129 Considering that the observed density gradient of laminin α5 and 332 from the retinal centre to the
130 far periphery corresponds to the visual angle, we wondered if there is any direct relationship between
131 this density gradient and the ability of RPE to bind and phagocyte POS. In fact, RPE phagocytic activity
132 naturally follows the visual angle, with the highest number of photoreceptors per RPE cell in the centre
133 and decreasing towards the periphery (Volland *et al*, 2015). Hence, we tested the ability of RPE
134 monolayers on PAA gels to bind and phagocyte POS fragments, which were isolated from porcine
135 eyes and fluorescently labelled with FITC (Fig. 2 E - G). The quantification shows that, overall, at high
136 laminin coating (10 - 30 µg/ml) there is a comparable efficiency of phagocytosis between laminin 332
137 and 511, whereas a divergency could be detected at the concentration of 5 µg/ml with reduced
138 efficiency of RPE on laminin 511 (~50 %) (Fig. 2 F, G).

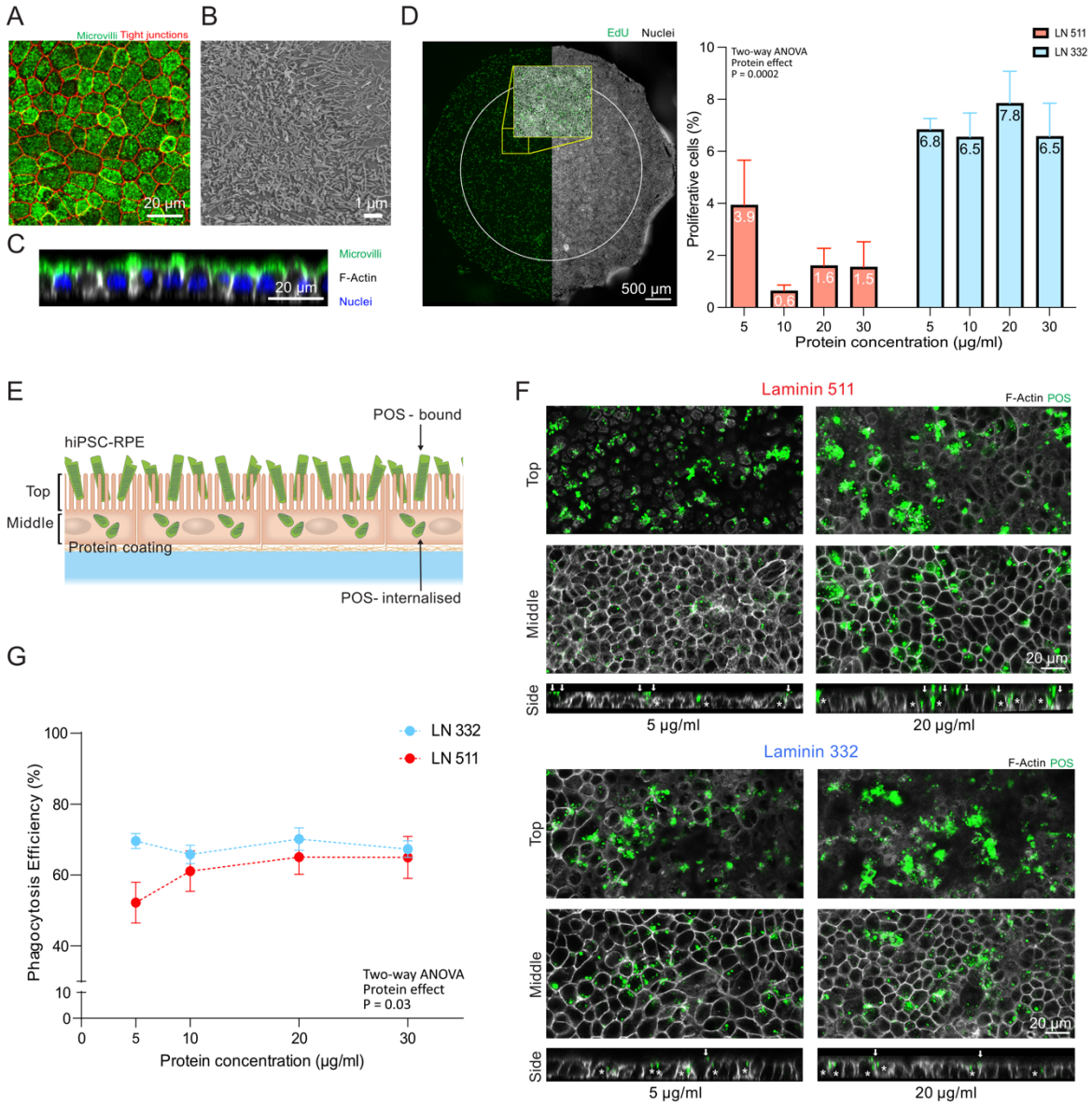

Figure 2: Human-relevant in vitro system for characterisation retinal mechanobiology. *hiPSC-derived RPE obtained on PAA gel with Young's modulus of 4 kPa coated with laminin 511 or laminin 332 in the presence of collagen type IV. After one week in culture, cells develop tight junctions (ZO-1) and apical microvilli (Ezrin) observed in a confocal cross section* ***(A)*** *and a scanning electron micrograph of the monolayer surface* ***(B)****.* ***(C)*** *Orthogonal projection of hiPSC-derived RPE epithelium displays a polarised monolayer with microvilli localised at the apical side of the cells.* ***(D)*** *Cellular proliferation rate obtained using EdU labelling assay on the surface of the PAA gel. Representative picture of the gel overview indicates the number of proliferating cells within one gel (left). The ratio of nuclei with incorporated EdU (per cent of proliferative cells) was quantified by the fluorescent signal in the central region of the gel (white circle). The data show average values ± SEM from at least 4 independent experiments. Statistics was performed using a mixed-effects model (REML) with the Geisser-Greenhouse correction, Tuckey's multiple comparisons test.* ***(E)*** *Schematic representation of the photoreceptor outer segment internalisation assay on one-week-old RPE monolayer.* ***(F)*** *Representative confocal images of the hiPSC-RPE cells on PAA hydrogel with laminin 511 or laminin 332 coating (in the presence of collagen type IV). The top row indicates FITC-labelled POS fragments at the apical surface of the cells. The middle row represents an optical section of the cell monolayer with POS fragments inside. The results of the POS phagocytosis assay are visible in the orthogonal projections (bottom row) where arrows and stars indicate bound and internalised POS respectively.* ***(G)*** *Average phagocytosis efficiency ± SEM for different laminin isoforms and their coating conditions from at least 4 independent experiments. The phagocytosis efficiency is defined as the amount of internalised POS divided by total POS. Statistical significance was tested using a mixed-effects model (REML) with the Geisser-Greenhouse correction, Tuckey's multiple comparisons test.*

140 In conclusion, hiPSC-RPE cells form a mature and functional monolayer on laminin 332 or 511 but not
141 on laminin 211 (with or without the addition of collagen type IV), excluding its major role in promoting
142 adhesion on Bruch's membrane for RPE. Furthermore, the phagocytosis assay revealed a reduction of
143 efficiency in internalising POS in RPE monolayers obtained with the lowest laminin 511 concentration.
144

145 Laminin density influences contractility levels in RPE monolayers

146 The quantification of RPE cell organisation and topological analyses in the retina suggested a direct
147 relationship between laminin density in the basement membrane and monolayer mechanical status.
148 Hence, following the logic of a comparative approach between the observation in the retina and the
149 *in vitro* system, we performed morphometric and topological analyses of the monolayers obtained on
150 the different laminin isoforms and densities (Fig. 3 A - C, sup. fig. 3 A - C). The calculation of the
151 average cellular area, perimeter, elongation and neighbourhood expresses a stable relationship
152 among all laminin densities and types, excluding their direct role in controlling monolayer topology.
153 Nevertheless, we wondered if those parameters may affect monolayer contractile forces. Hence, we
154 used traction force and monolayer stress microscopy to quantify RPE cell-matrix traction forces and
155 cell-cell stresses in different conditions (Fig. 3 D - G). The quantifications revealed an overall ability of
156 laminin 511 to promote higher traction forces compared to laminin 332 (Fig. 3 D, E). Interestingly, as
157 observed for the phagocytosis efficiency, the highest difference of average traction force (170 Pa vs
158 80 Pa) was recorded at the lowest laminin density (5 µg/ml) (Fig. 3 E). Next, we used the information
159 on the traction forces and monolayer height (Sup. fig. 3 D) to calculate intercellular stresses at the
160 different conditions as previously shown (Di Russo *et al*, 2021; Vishwakarma *et al*, 2018) (Fig. 3D, F, G).
161 Also, in this case, we observed a significant difference in the overall monolayer absolute stresses at
162 the lowest concentration of laminins (5 µg/ml) with an average of ~1 Pa for laminin 511 and 0.6 Pa for
163 laminin 332 (Fig. 3 G). As expected, overall, the stress vectors are averaging close to 0 Pa for both
164 coating and densities, indicating that monolayers are in a state of near equilibrium despite the
165 difference in absolute contractility (Fig. 3 F). The difference in traction and stress quantified at the
166 lowest concentration of laminin 511 might be caused by a gradual increase of cell adhesion to collagen
167 type IV, which was kept constant through the conditions. Therefore, we tested the effect of collagen
168 type IV on monolayer traction forces using laminin 332 as control, since laminin 511 alone does not
169 support the formation of a monolayer (Sup. fig. 2 A). The quantification shows an overall decrease (~
170 40%) of traction in the presence of collagen type IV (Sup. fig. 2 E), clearly excluding the role of collagen
171 type IV for the observed increased traction at the lowest laminin 511 density. Moreover, the distinct
172 variation between laminin 511 and laminin 332 mediated traction strengthens the conclusion that the
173 observed changes are laminin-induced. Finally, we wanted to understand if the coating density could

174 generally impact RPE cell surface stiffness, which may affect POS adhesion and phagocytosis.
175 Therefore, we indented RPE cells within the monolayers using a spherical probe of approximately 10
176 µm radius and quantified the average Effective Young's modulus of the monolayers (Fig. 3 H). The data
177 show that RPE monolayers on laminin 511 are stiffer (~1.5 kPa) than on laminin 332 (~1 kPa) regardless
178 of the protein surface density, thus excluding the effect of cellular stiffness for POS phagocytosis
179 efficiency.

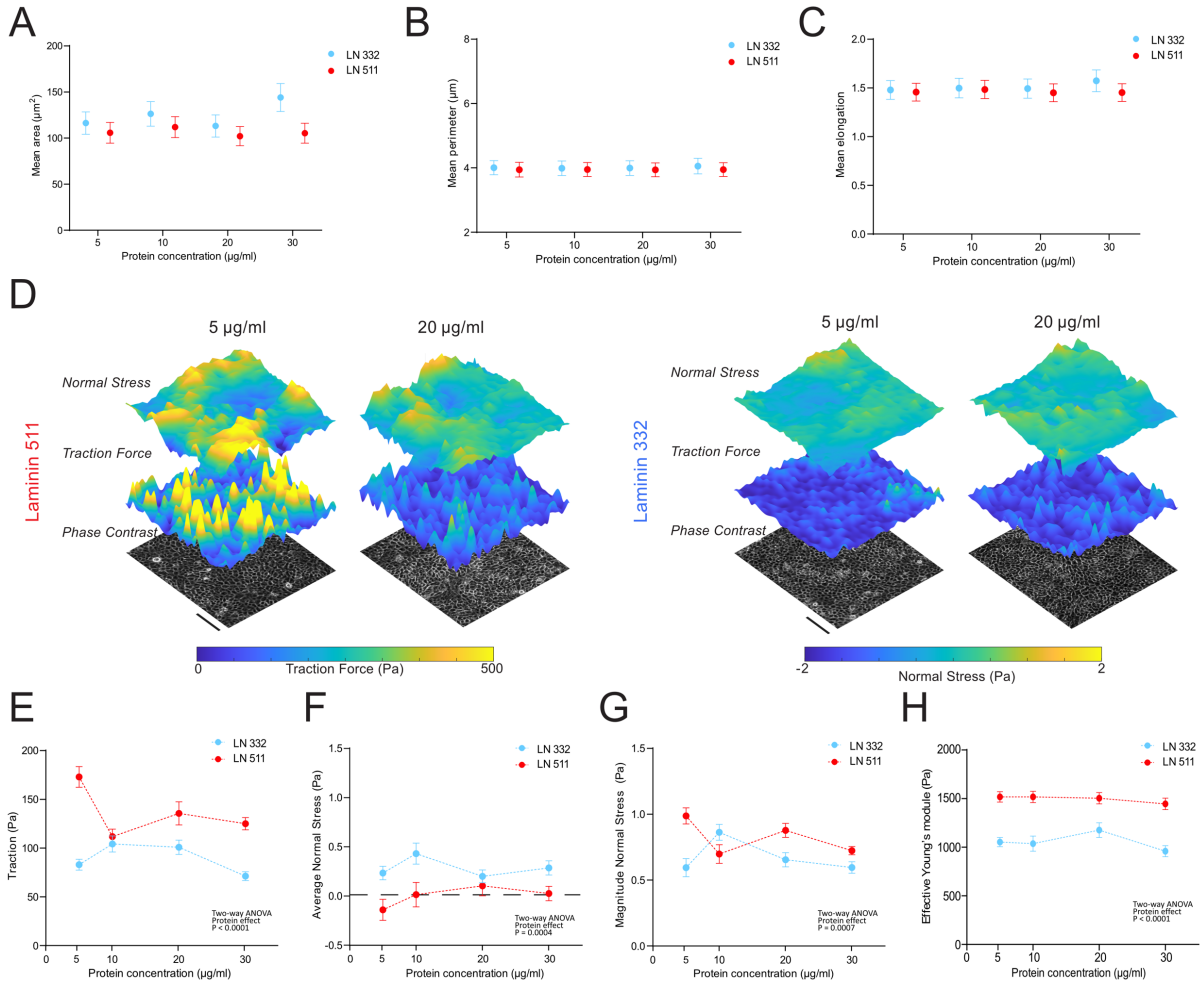

Figure 3: Laminin surface density affects the contractility of RPE monolayers. *The morphometric analysis reveals the absence of significant difference in cellular mean area* ***(A)****, mean perimeter* ***(B)*** *and mean elongation* ***(C)*** *between different laminin isoforms and densities from 3 independent experiments.* ***(D)*** *Representative traction force and monolayer stress profiles for different coating conditions and their quantifications* ***(E, F and G)*** *show a significant increase in contractility of RPE monolayers at the lowest laminin 511 coating.* ***(H)*** *Quantification of the effective Young's modulus of the apical side of monolayer in different conditions. Data are shown as average ± SEM from at least 4 independent experiments. Statistical analyses were performed using a mixed-effects model (REML) with the Geisser-Greenhouse correction, Tuckey's multiple comparisons test.*

180 In conclusion, the biomechanical characterisation of our model clearly indicates a direct effect of the
181 low density of laminin 511 on the overall RPE mechanical equilibrium with increased contractility of the
182 monolayer.
183

184

185 Overall monolayer traction force modulates RPE functionality

186 Epithelial contractility levels have been shown to directly influence tissue functionality and reactivity
187 (Vishwakarma *et al*, 2018; Di Russo *et al*, 2021; Park *et al*, 2015; Malinverno *et al*, 2017; Palamidessi *et*
188 *al*, 2019; Balcioglu *et al*, 2020; Mongera *et al*, 2018; Pérez-González *et al*, 2021). Thus, we asked
189 ourselves if the efficiency of RPE to phagocyte POS is generally affected by the level of monolayer
190 traction forces independently of the biochemical nature of ECM adhesion, i.e., laminin isoforms or
191 density. This is also suggested by comparing traction forces with POS phagocytosis efficiency
192 independently of the surface coating (Fig. 4 A). To systematically modify the level of traction force, we
193 decided to tune either the ECM physical cues (i.e., hydrogel stiffness) or the biochemical nature of
194 adhesion (i.e., laminins vs vitronectin) (Fig. 4 B) and compare RPE efficiency in internalising POS with
195 the maximum efficiency observed in RPE on laminins. First, we obtained RPE monolayers on stiffer
196 hydrogels (18 kPa) coated with laminin 511 or 332 (20 µg/ml) in the presence of collagen type IV (30
197 µg/ml), which developed a significantly increased traction force (~140 Pa and ~170 Pa respectively).
198 This corresponded to reduced efficiency of these monolayers to internalise POS (~ 40%) (Fig. 4 C, D).
199 Second, we measured the phagocytotic activity and traction forces of monolayers obtained on 4 kPa
200 stiff hydrogels coated with a high concentration of vitronectin (250 µg/ml) (Fig. 4 C, D). Also, in this
201 case, the analyses revealed a higher average traction force (~ 200 Pa) which corresponded to a reduced
202 ability of RPE to internalise POS (~ 40%). To distinguish the exclusive role of cellular contractility from
203 the possible converging effects of ECM signalling, we inhibited or induced actomyosin contractility in
204 RPE monolayers using a ROCK inhibitor or a RhoA activator (Fig. 4 B, E). The reduction of contractility
205 was performed on RPE monolayers cultured on soft (4 kPa) surfaces coated with collagen type IV (30
206 µg/ml) with little addition of laminins (2.5 µg/ml) which showed *per se* a low activity for POS
207 phagocytosis (~ 50%). On the other hand, the increase of contractility was induced in RPE on high
208 density laminins (20 µg/ml) in the presence of collagen type IV. The quantification revealed a direct
209 connection between actomyosin contractility and monolayer efficiency in POS phagocytosis.
210 Independently of the laminin type, RPE phagocytic efficiency increased after ROCK inhibitor treatment
211 (from ~50% to ~70%) and decreased after RhoA activator treatment (from ~70% to ~50%) (Fig. 4 F).
212 As expected, the drug treatments also affected the ability of RPE to develop traction forces with
213 reduced traction after ROCK inhibitor treatment and increased after RhoA activation (Fig. E).

214 Overall, these data show the direct influence of RPE contractility on its ability to phagocyte POS.
215 Interestingly, this effect is independent of the nature of adhesion and thus can be influenced by both
216 biochemical and physical cues from the ECM.

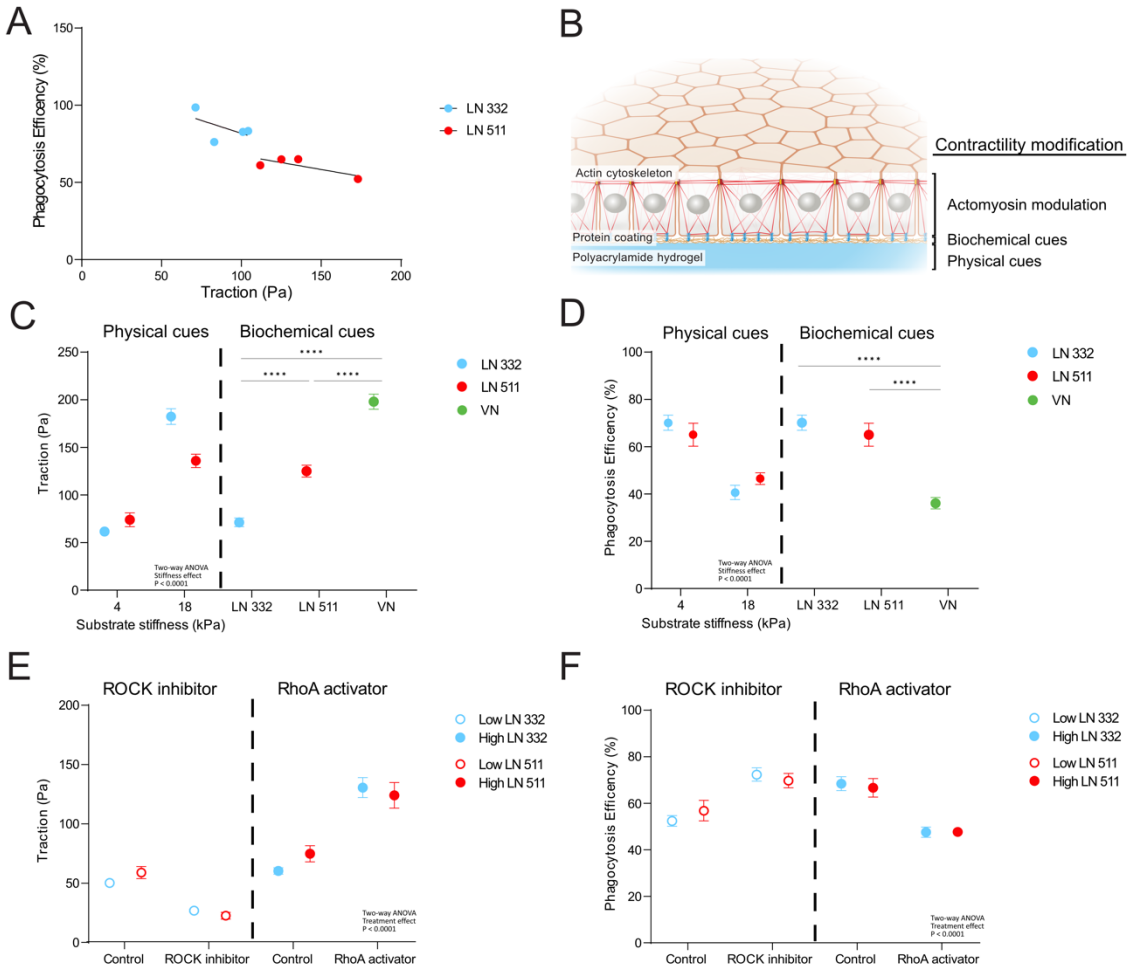

Figure 4: Overall monolayer contractility modulates the cellular functionality. ***(A)*** *Relation between the RPE phagocytosis efficiency and traction forces independently of surface coating.* ***(B)*** *Schematic representation of the experimental strategy to interfere with monolayer contractility. Quantification of mean traction forces* ***(C)*** *and phagocytosis efficiency* ***(D)*** *±SEM in RPE upon different ECM physical (stiffness) and biochemical cues (coating). PAA gels were coated with laminin 511 (LN 511) or laminin 332 (LN 332) (in the presence of collagen type IV) or with vitronectin (VN). ****p<0.0001 using mixed-effects model (REML) with the Geisser-Greenhouse correction, Tuckey's multiple comparisons test (physical cues) and Mann-Whitney test (biochemical cues). Drug treatment, affecting actomyosin contractility levels, using ROCK inhibitor and RhoA activator shows inverse dependence between the level of monolayer contractility (traction forces)* ***(E)*** *and its ability to phagocyte POS fragments* ***(F)****. Data are shown as mean ± SEM. ****p<0.0001 using mixed-effects model (REML) with the Geisser-Greenhouse correction, Tuckey's multiple comparisons paired test.*

217

DISCUSSION

Our findings demonstrate the unknown direct role of laminin alpha 5 density in regulating RPE mechanical homeostasis. For the first time, we report the presence of a relative density gradient of specific laminin isoforms in the Bruch's membrane. At the retinal centre, the Bruch's membrane contains the highest density of laminins, whereas at the far-periphery, the laminin 332 and alpha 5-containing isoforms have the lowest density (Fig. 1J). This laminin density gradient correlates with a gradual increase of RPE cellular shape factor with lower laminin density corresponding to more elongated cells (Fig. 1 B, C, sup. fig. 1 D, E). Furthermore, the topological analyses suggest a variation along the visual axis (Fig. 1 E, F, sup. fig. 1 I, J). Cellular shape factor and cell-to-neighbourhood relationship directly correspond to mechanical properties of the epithelial monolayers (Hannezo *et al*, 2014; Alt *et al*, 2017; Kaliman *et al*, 2021) and contractility (Park *et al*, 2015; Bi *et al*, 2015; Vishwakarma *et al*, 2018). Hence, it is highly probable that a higher contractility is present at the far periphery (elongated cells) in contrast with the centre (honeycomb organisation).

Due to technical limitations for a direct quantification of mechanical properties and contractility *in vivo*, it was required for us to establish a complementary approach. Therefore, we established an *in vitro* model using laminin-functionalized PAA gels and hiPSC-derived RPE cells. The stringent condition for ECM availability and remodelling created by the PAA gel revealed a direct role of low-density laminin 511 in increasing RPE contractility (higher traction forces and monolayer stress) and reducing the epithelium efficiency to phagocyte POS. Despite the increase in contractility of RPE on the low density of laminin 511, we did not observe a change in cell shape or in topology. This suggests that the monolayer topology and morphology *in vivo* may be defined by the convergence of several factors. At the far periphery RPE is anchored to the ora serrata with complex intercellular connections (Nobeschi *et al*, 2006). In combination with monolayer contraction, this possibly causes the observed topological variation. Moreover, our data rule out the exclusive role of laminins in defining RPE monolayer organisation.

The effect of laminin alpha 5 on cellular mechanics is not surprising. Laminin alpha 5 containing isoforms have been shown to enhance cell stiffness and support better shear stress mechanotransduction (Di Russo *et al*, 2016) and intercellular tightness (Song *et al*, 2017) in the endothelium. In fact, in comparison with other laminin chains, the N-terminal region of laminin alpha 5 contains arginine - guanidine – aspartate sequences (RGD) that can support the adhesion of non-classical laminin receptors, including $\alpha v\beta 1$ and $\alpha 5\beta 1$ integrins. The engagement of integrin $\alpha 5\beta 1$ induces downstream activation of RhoA and ROCK, thus supporting an increased myosin II activity and overall cell contractility (Schiller *et al*, 2013; Di Russo *et al*, 2016). Furthermore, the density of RGD-mediated adhesion has been shown to define cellular traction forces and contractility, with the highest

contractility corresponding to low density (Oria *et al*, 2017). The low density of the laminin alpha 5 chain may therefore support an overall increase in contraction due to RGD-mediated adhesion. This can also explain why RPE cultured on low density of laminin 332 does not increase contractility, since it lacks RGD sequences. Nevertheless, due to our *in vitro* model's limitations, we cannot completely exclude the role of laminin 332 in controlling RPE mechanical status. In fact, laminin 332 supports the formation of hemidesmosomes (Aumailley, 2012), which are well-known key ECM receptors controlling epithelial mechanical integrity and resilience(Hahn & Labouesse, 2001; Todorović *et al*, 2013). Future studies will need to focus on elucidating the potential ECM receptor density gradient in RPE *in vivo* and its role in the mechanical homeostasis of the outer retina.

A study on stem-cell derived RPE has previously shown that the organisation of the actin cytoskeleton can predict the ability of differentiated cells to phagocyte POS (Müller *et al*, 2018). Particularly, the presence of F-actin stress fibres impaired the phagocytic activity of these cells. These data, together with our findings, strongly suggest that high contractility in RPE is detrimental to its homeostasis and function. RPE apical microvilli interact with POS mostly via the Mer tyrosine kinase receptor (MerTK) and the integrin $\alpha v\beta 5$ (Kwon & Freeman, 2020). The activation of MerTK is thought to be involved in the inside-out activation of integrin $\alpha v\beta 5$ with the recruitment of talin, vinculin and interaction with F-actin (Kwon & Freeman, 2020). These focal adhesion-like structures have already been shown to mediate phagocytosis in macrophages and to be mechanosensitive (Jaumouillé *et al*, 2019). Hence, the formation of this apical molecular clutch may be sensitive to the overall cellular contractility defined by the ECM substrate and explains the lower efficiency of POS internalisation observed in this work. Furthermore, the neural cell adhesion molecule (N-CAM) homophilic interaction between POS and RPE may also be affected by increased RPE contractility affecting the bond lifetime, thus, binding efficiency.

Overall, our work underlines the important role of RPE mechanobiology for outer retina physiology and opens important questions about its role in retinal ageing. Remodelling of the ECM during ageing may shift RPE mechanical homeostasis out of its optimal range, making it more prone to phenotypical changes. Overcoming this threshold may cause sight-impairing diseases such as (high) myopia and age-related macular degeneration. Nevertheless, further studies will be necessary to elucidate to what extent RPE contractility is involved in outer retina diseases.

CONTRIBUTIONS

J.D.R. conceived the project. A.N.K. and T.P. designed and performed all the experiments. I.D. and F.S. helped in establishing hiPSC-derived RPE cell culture on PAA gels. T.Pr. and L.S.Y. supported image segmentations and analyses. T.H. performed and analysed AFM experiments on decellularised

286 Bruch's membrane. M.H. and A.S. contributed to morphometric analyses and interpretation of RPE
287 monolayers *in vivo* and *in vitro*. J.D.R., A.N.K. and T.P. wrote the manuscript, and all authors discussed
288 and commented on it.
289
290 ACKNOWLEDGMENT
291 This work was supported by a grant from the Interdisciplinary Centre for Clinical Research within the
292 Faculty of Medicine at the RWTH Aachen University and from the German Research Foundation
293 - DFG - (grant n° RU 337 2366/3-1). Furthermore, the authors acknowledge the support of the
294 mechanobiology in epithelial 3D tissue constructs (ME3T) graduate school (GRK 2415/363055819) and
295 the DWI – Leibniz-Institute for Interactive Materials. We would like to thank Rudolf Leube for the critical
296 discussions of the data. Finally, we are grateful for Gloria's excellent technical support in imaging.
297
298 METHODS
299 **Retina flat mount preparation.** Retina flat mounts were prepared from BALB/c mice of 25-30 weeks of
300 age. After sacrifice, the eyes were enucleated and fixed with 2% (wt/vol) paraformaldehyde (PFA) for
301 4 hours at 4°C rotating. To best visualize the RPE layer, the eyes were prepared as flat mounts
302 according to published protocol (Claybon & Bishop, 2011). Briefly, the cornea, the iris and the lens
303 were removed, and the eyecup was cut into eight longitudinal slices to allow its spreading. Afterwards,
304 the neurosensory retina was gently detached exposing the RPE layer adhering to its ECM for
305 fluorescent staining and imaging. The animal care and sacrifice were conducted according to the
306 German Animal Welfare Act (LANUV, reference number 84- 02.04.2015.A190).
307
308 **Atomic force microscopy of Bruch's membrane.** Upon enucleation, murine eyes were freshly dissected
309 using cold phosphate-buffered saline without Ca^{2+} and Mg^{2+} ($PBS^{-/-}$) and containing proteinase
310 inhibitors as instructed by the manufacturer (Roche). Dissected eyes were denuded by the RPE layer
311 via incubation of the tissue for 60 minutes with 50 mM Tris–HCl buffer plus 20 mM ethylenediamine
312 tetraacetic acid (EDTA), pH 7.4, followed by 20 minutes incubation in 50 mM Tris–HCl buffer and two
313 washes of 10 minutes with 1 M NaCl, pH 7.4. Each solution contained freshly added proteinase
314 inhibitors (Roche). Next, the prepared eyes were glued to a surface using Cell-Tak Cell and Tissue
315 Adhesive (Corning, 354240). Cantilevers with a spherical colloidal tip of 6.62 µm diameter (Nano and
316 More GmbH, CP-PNPS-SiO-C-5) were used to indent 200 nm into the decellularised Bruch's
317 membrane in different regions of the eye. The experiments were performed in a Dimension Icon atomic
318 force microscope (Bruker Co. USA). Probes were calibrated using the thermal oscillation method, built
319 into the software (Nanoscope 9.4). Force distance curves were recorded with an approach and

320 retraction speed of 1 µm/s, with a relative maximal force set typically to 2 nN. The maximal range of
321 the Z-piezo was set to 2.5 µm. All curves were exported to ASCII files with the analysis software of the
322 instrument. The approach part of the curves is analysed using a custom-written script in Python
323 (https://www.python.org) using the Hertz model (equation (1)). The Poisson ratio was assumed to be
324 v = 0.3. The last 40-50% of the data points are fit to a line and subtracted as background.
325
326 $$F(\delta) = \frac{4}{3}\frac{E}{1-v^2}\sqrt{R}(\delta - \delta_0)^{3/2} \qquad (1)$$
327
328 The model fits the whole curve using a nonlinear fit (leastsq) from Scipy (https://www.scipy.org) finding
329 both Young's modulus and the contact point.
330
331 **Immunofluorescence of retinal tissue.** Fluorescent staining of retina flat mounts was performed as
332 follows. After fixation and dissection, the tissue was incubated for one hour in 1% bovine serum
333 albumin (BSA) (wt/vol) in PBS containing 0.1% (vol/vol) Triton X-100, followed by overnight staining at
334 4°C with primary antibodies or phalloidin dissolved in PBS solution of 1% (wt/vol) BSA and 0.1%
335 (vol/vol) Triton X-100. Secondary antibodies were diluted in PBS containing 0.1% (vol/vol) Triton X-100
336 and incubated with the tissue at room temperature for two hours. Finally, the retinas were incubated
337 for 15 minutes with 5 µg/ml Hoechst 33342 (Thermo-Fischer Scientific, 62249) in PBS before being
338 mounted on glass slides with Mowiol mounting medium (Sigma-Aldrich). Primary and secondary
339 antibodies used in this work are listed in supplementary table 1.
340
341 **Retinal extracellular matrix quantification.** To quantify the relative amount of ECM protein in the
342 Bruch's membrane, upon immunofluorescence staining, Z-stacks (0.5 µm optical slices) from the
343 different regions were obtained using a Zeiss LSM 710 (Carl Zeiss) confocal microscope using unified
344 illumination settings. The distance from the optic nerve was monitored by using the automated stage
345 of the microscope and by setting the optic nerve as an origin. Within the eye, Z-stacks for each region
346 were recorded per eight longitudinal slices, respectively. Mean fluorescent intensity in single optical
347 sections identified as BrM was measured using Fiji software (National Institutes of Health, USA).
348 Manually-defined regions of interest (ROIs) were chosen to avoid artefacts due to tissue tearing during
349 preparation (Fig. 1 I "stars"). Three to five ROIs were measured for each stack, and the fluorescence
350 intensity of all data was normalized to the highest measured value in the eye.
351
352 **hiPSC-RPE culture.** Differentiated hiPSC-RPE were purchased cryopreserved from FUJIFILM Cellular
353 Dynamics and after thawing, seeded in 24-well plates coated with 2.5 µg/ml Vitronectin XF (StemCell

354 Technologies, 07180) at a density of 1600-1800 cells/mm^2. Cells were cultured to confluence in a
355 humidified incubator at 37°C and 5% CO_2 and then, after detachment, reconstituted in
356 CELLBANKER 2® freezing media (Amsbio LLC, 11891) and kept in liquid nitrogen for future use. Cell
357 detachment for cryopreservation or experiments was achieved through 30 minutes of incubation with
358 5 mM EDTA in PBS$^{-/-}$ followed by TrypLE Express dissociation agent (Gibco, 12605-010) for five minutes
359 at 37°C. Prior to seeding, cells were centrifuged at 300 g for 5 minutes and resuspended in the media
360 at the desired density. For the experiments, cells were thawed again and cultured for one to two weeks
361 to confluence before use. For seeding on polyacrylamide hydrogels, cells were seeded at a density of
362 5000-6000 cells/mm2, corresponding to the RPE density in the human macula (Bhatia *et al*, 2016) and
363 cultured for one week. Cells were cultured in hiPSC-RPE medium composed of MEM α, nucleosides
364 (Thermo Fisher, 12571-063), 5% (vol/vol) knock-out serum replacement (Gibco, 10828-028), 1%
365 (vol/vol) N-2 supplement (Gibco, 17502-048), 55 nM hydrocortisone (Sigma-Aldrich, H6909), 250
366 µg/ml taurine (Sigma, T0625), 14 pg/ml triiodo-L-thyronine (Sigma, T5516) and 25 µg/ml gentamicin
367 (Gibco, 15750-060). The medium was exchanged every second day.
368
369 **Hydrogel preparation and functionalisation.** To obtain flat hydrogel substrates, a mixture of 40%
370 acrylamide (Bio-Rad, 1610140) and 2% bis-acrylamide (Bio-Rad, 1610142) in distilled water was first
371 prepared. The following ratios of acrylamide / bis-acrylamide in the mixture were used to reach
372 different hydrogel Young's moduli quantified by nanoindentation: 5 % / 0.1 % (wt/vol) for 4 kPa and
373 10% / 0.07 % (wt /vol) for 18 kPa. Then, the mixture was combined with 0.5 % of (vol/vol) ammonium
374 persulfate (Sigma Aldrich, 248614, 10 % (wt/vol) stock solution in distilled water) and 0.05 % (vol/vol)
375 N`-tetramethylethylenediamine (Sigma Aldrich, 411019), and pipetted between glutaraldehyde -
376 activated glass bottom petri dishes (Cellvis, D35-20-0-N) and a hydrophobic glass coverslip. If
377 hydrogels were used for traction force microscopy, 1 µm yellow-green carboxylate-modified
378 polystyrene microbeads (Sigma, L4655) were included in the solution. ECM proteins were crosslinked
379 on the hydrogels' surface according to the protocol described by Przybyla L. and colleagues (Przybyla
380 *et al*, 2016). Briefly, for functionalisation solution, we prepared stocks of 0.5 M HEPES NaOH pH6 and
381 0.2% (wt/vol) bis-acrylamide in distilled water, 0.2 % (vol/vol) tetramethacrylate (Sigma, 408360) and
382 3% (wt/vol) hydroxy-4'-(2-hydroxyethoxy)-2-methylpropiophenone (Sigma, 410896) in ethanol. Acrylic
383 acid N-hydroxysuccinimide ester (Sigma, A8060) was initially dissolved in DMSO (0.03 % (wt/vol)) and
384 later reconstituted in 50% ethanol for the final concentration of 0.0003% in the functionalisation
385 solution. Calculating 0.5 ml solution per gel, we combined 216.65 µl of sterile water, 50 µl of 0.5 M
386 HEPES NaOH pH 6, 32.5 µl of ethanol and 25 µl of bis-acrylamide and degassed under vacuum for 20
387 min. Then, 5 µl tetramethacrylate, 4.165 µl hydroxy-4'-(2-hydroxyethoxy)-2-methylpropiophenone and

388 5 µl of ester in 161.65 µl of 50% ethanol were added to the degassed solution. The completed
389 functionalization solution was applied over the surface of hydrogels, previously partly dehydrated in a
390 70% ethanol solution, and the hydrogels were exposed for 10 minutes to ultraviolet light. After double
391 washing with 25 mM HEPES buffer and $PBS^{-/-}$ for a total of 20 minutes, the gel surface was incubated
392 overnight at 4°C with the desired ECM protein solution. Human recombinant Laminin-511 (Biolamina,
393 LN511-0202) and Laminin-332 (Biolamina, LN332-0202) were prepared at the desired concentration in
394 PBS containing Ca^{2+} and Mg^{2+} ($PBS^{+/+}$) mixed with 30 µg/ml Collagen type IV (Sigma-Aldrich, M7027-
395 100G). Vitronectin (StemCell Technologies, 07180) was used without dilution at 250 µg/ml. Finally, the
396 obtained hydrogels were sterilized by 30 min ultraviolet light irradiation before their application as cell
397 culture substrates.
398
399 **Immunofluorescence staining of hiPSC-RPE.** Cells on hydrogels were first quickly washed with warm
400 (~37 °C) PBS containing Ca^{2+} and Mg^{2+} ($PBS^{+/+}$) then fixed with warm (~37 °C) 2% (wt/vol) PFA for 8
401 minutes at room temperature. After fixation, cells were permeabilized with 0.3% (vol/vol) Triton X-100
402 for 2 minutes and blocked with 1% (wt/vol) BSA for 30 minutes at room temperature. Primary
403 antibodies or Phalloidin-iFluor 647 Reagent (ab176759) in PBS containing 1% (wt/vol) BSA were
404 incubated overnight at 4°C. The following day, secondary antibodies were diluted in a PBS solution
405 containing DAPI (1 µg/ml, Invitrogen D1306) and incubated with the sample for 30 minutes at room
406 temperature. Primary and secondary antibodies used in this work are listed in supplementary table 1.
407 The samples were imaged in PBS solution to match the immersion type of the objective. Both stained
408 retinas and cells were imaged using Plan-Apochromat 40x water immersion objective on Zeiss LSM
409 710 confocal microscope with Airyscan capability (Carl Zeiss).
410
411 **Live staining.** For live imaging of F-actin, hiPSC-RPE cells cultured on PAA gels were incubated with 1
412 mM of a fluorogenic F-actin probe SirActin (Spirochrome, SC001) containing medium for at least two
413 hours before imaging. The samples were imaged using Plan-Apochromat 40x water immersion
414 objective on Zeiss LSM 710 confocal microscope with Airyscan capability (Carl Zeiss). Orthogonal views
415 from Z-stacks obtained after confocal live imaging of F-actin (SirActin) were used to measure the
416 average junctional height of RPE monolayers in culture using Fiji image processing package (National
417 Institutes of Health, USA).
418
419 **Scanning Electron Microscopy** (Critical Point Drying). After a week in culture on a polyacrylamide gel
420 with the defined coating, hiPSC-RPE were fixed in 3% glutaraldehyde (Agar scientific, Wetzlar,
421 Germany) for 4 h at 4°C followed by a washing in 0.1 M Soerensen's Phosphate Buffer (Merck,

422 Darmstadt, Germany). The dehydrating step was performed in the ascending alcohol series with 10
423 minutes duration each. The samples were sequentially immersed in the following solutions : 30%
424 ethanol, 50% ethanol, 70% ethanol, 90% ethanol, and three times in 100% ethanol. Critical Point
425 Drying was performed in liquid CO2. Prior to imaging, cell monolayers were coated with 10 nm
426 gold/palladium layer.
427
428 **Photoreceptor outer segment internalisation assay**. Photoreceptor outer segments (POS) were isolated
429 in batches from porcine eyes from a local slaughterhouse as previously described (Parinot *et al*, 2014).
430 Briefly, the eyes were dissected using a red safelight lamp as the only illumination source, and the
431 neural retina was collected. After retinal mechanical homogenisation, POS were isolated via
432 ultracentrifugation in a sucrose gradient. Thereafter, POS were labelled with 2.5 mg/ml FITC dye
433 (Thermo Fisher, F1906), resuspended in DMEM (Thermo Fisher, 31331-028) containing 2.5% sucrose
434 and stored in aliquots at -80 °C for future use. For internalisation assay, POS aliquots were thawed in
435 a water bath, washed with medium, centrifuged at 2300g for 5 min and resuspended in hiPSC-RPE cell
436 medium to an amount of roughly 10 POS per RPE cell in culture. Human MGF-E8 protein (R&D
437 Systems, 2767-MF-050) and human protein-S (Coachrom, pp012A) were added at respectively
438 2.4 µg/ml and 2 µg/ml to aid the internalisation. Next, hiPSC-RPE monolayers were washed twice with
439 warm media and incubated for four hours at 37°C with the prepared mixture at a density of
440 approximately ten POS per cell. After incubation, the monolayers were washed four times with warm
441 $PBS^{+/+}$ and fixed for fluorescence staining as described. Phagocytosis efficiency was calculated as
442 projected area of internalised POS divided by the total projected POS area in the same field of view.
443 Internalised POS were identified in orthogonal views from confocal optical sections (0.5 µm) by using
444 F-actin staining to distinguish between apical-bound and internalised segments. Analyses were
445 automatised with the particle analyses plugin of Fiji software (National Institutes of Health, USA) after
446 applying a binary mask on the images.
447
448 **Proliferation assay.** Levels of proliferation in hiPSC-RPE monolayers were assessed using a proliferation
449 assay kit Click-iT EdU (Thermo Fisher, C10337). Cells were incubated with a 1:1 mixture of cell culture
450 supernatant and 5-Ethinyl-2'-Desoxyuridin (EdU) (20 µM) containing hiPSC-RPE cell culture medium for
451 24 h. Final EdU concentration in the mixture was 10 µM. Afterwards, cells were fixed as described for
452 immunofluorescent labelling and processed according to the manufacturer's instructions. As EdU
453 incorporates into newly synthesized DNA, proliferating cells were identified as having their nucleus
454 positively stained with EdU-Alexa Fluor 488. The total area of the gel was imaged on Axio Observer 7
455 (Carl Zeiss) microscope as an overview using the tiles option. The ratio of proliferating cells was

456 calculated in comparison with DAPI-positive nuclei and quantified using the particle analysis plugin of
457 Fiji software (National Institutes of Health, USA).
458
459 **Drug experiments.** For activation of the RhoA-dependent pathways, we incubated RPE monolayers
460 with Rho activator II (Cytoskeleton, CN03-A) and Rho kinase (ROCK) inhibitor Y-27632 (Sigma Aldrich,
461 Y0503) (https://doi.org/10.3390/cells10081927). Briefly, the one-week-old RPE monolayers on a
462 hydrogel coated with high laminin concentration (20 µg/ml) were treated with Rho activator II (1 µg/ml)
463 containing media for 3 hours prior to POS phagocytosis assay or traction force measurements to
464 promote the actomyosin contractility, or with an equal volume of water as a solvent control. To reduce
465 the actomyosin contractility at low laminin surface concentration (2.5 µg/ml), ROCK inhibitor (25 µM)
466 was added to the media one hour prior the POS phagocytosis assay or traction force measurements.
467 An equal volume of DMSO was used as a solvent control. Further analysis was performed as described
468 in the relevant chapters.
469
470 **Morphometric and topology analyses.** Microscopy images of RPE *in vivo* and *in vitro* were segmented
471 using the cellpose software (Stringer *et al*, 2021) (www.cellpose.org) applied on F-Actin micrographs.
472 Segmented cells were imported into Fiji as ROIs and used to generate skeletonised images. The
473 skeletonised images were then imported into custom-written MATLAB software (Kaliman *et al*, 2016).
474 Prior to analysis, the software removes 15 pixels on the sides of the images to remove poor mask
475 definition by cellpose (Sup. fig. 1 B), and then applies a gaussian filter with a standard deviation of 2
476 pixels (function "imgaussfilt") to correct the pixel connectivity on the masks provided by cellpose.
477 Finally, the software extracts information about the cell morphology (cell area, perimeter, and
478 elongation) and topology (cell neighbours) as previously described (Kaliman *et al*, 2016). For these
479 analyses, the cells at the edge of the picture were not considered to avoid any segmentation error
480 (Sup. fig. 1 C). For *in vivo* images, in total, 24 images from 3 different mice have been analysed for the
481 "centre" and "mid-periphery" regions of the retina (8 images each) and 23 images for the "far-
482 periphery" region (8-8-7 images for the 3 mice respectively). This corresponds to a total cell number
483 of 5575 cells for the centre, 7957 for the mid-periphery and 7863 for the far-periphery. For *in vitro*
484 images, 71 images were analysed (at least 2 images per experiment). Each image provided in between
485 86 and 312 cells. Because of segmentation error, to remove unnaturally large cells, cells with a rescaled
486 area (see below) higher than 2, and cells with a neighbourhood larger than 10 cells have been removed
487 from the analysis. The number of cells per condition is summarised in supplementary table 2. To build
488 both Lewis' and Desh' law, data were separated with respect to their number of neighbours and binned
489 in different classes before being averaged. To build Aboav-Weaire's law, the cells at the images' edge

were removed, since their neighbourhood is not defined. For that, the neighbourhood of each cell is reconstructed to determine the average position of the collection of neighbours. If the distance between their average position and the central cells is less than 30px, the central cell is assumed to be in the bulk of the image and not on the border of the image. To plot Aboav-Weaire's law, we computed b(n) defined in (2).

$$b(n) = (n-6)\mu_{m(n)} - \sigma_n^2 \qquad (2)$$

where $\mu_{m(n)}$ is the mean size of the neighbourhood among the neighbours, and σ_n^2 is the central second moment of the distribution of neighbours, i.e., its variance. Such distribution is taken for a given mouse, not among different mice. Data from the different mice are average together with a ponderation proportional to the total number of cells making the statistics.

Stiffness measurements of hiPSC-RPE monolayers. Measurements were performed using a Chiaro Nanoindenter System (Optics 11 Life) mounted on Zeiss Axio Observer 7 (Carl Zeiss) with an environmental chamber sustaining 37°C. A probe of 10 µm radius and 0.025 N/m stiffness (Optics 11 Life) was used and the indentation was performed in displacement control mode, indenting 10 µm into the cells monolayer. Approach curves were fitted via the DataViewer V2.4.0 software (Optics 11 Life) using a Hertz model according to a set indentation depth of 0 to 3 µm for the apical stiffness. A Poisson's ratio of 0.5 was used and a maximum load of 30% was allowed for setting the contact point. Only results from well fitted data ($R^2 > 0.95$) were considered for statistics.

Traction force and monolayer stress microscopy. Traction force quantification and monolayer stress calculations were performed as previously described (Di Russo *et al*, 2021; Vishwakarma *et al*, 2018). Briefly, a week-old monolayer cultured on a PAA gel substrate containing fluorescent beads was imaged using Axio Observer 7 (Carl Zeiss) microscope for the beads signal. Then, the monolayer was detached with 0.5% SDS solution in PBS followed by washing steps and 20 minutes of gel incubation in cell media to prevent gel shrinkage due to the solvent change. Positions of the fluorescent beads in the hydrogels after the detachment of cells (relaxed state of the gel) were compared to the tense gel state before and beads displacement vectors were calculated using the particle image velocimetry (PIV) plugin of Fiji (National Institutes of Health, USA). Traction forces were calculated from these vectors using the Fourier transform traction cytometry plugin (FTTC) of Fiji (National Institutes of Health, USA). Next, average normal stress vectors were calculated using the traction force information using a force balance algorithm in MATLAB (MathWorks) as formulated elsewhere (Di Russo *et al*, 2021;

523 Vishwakarma *et al*, 2018). For each measured sample, the average cell height was calculated using a
524 live actin staining (SirActin, Spirochrome) to correctly input the force balance algorithm.
525
526 **Statistics.** Statistical analysis was performed using Prism (GraphPad). Sample conditions and the
527 specific test used for each data set are indicated in corresponding figure captions.

REFERENCES

Aboav DA (1970) The arrangement of grains in a polycrystal. *Metallography* 3: 383–390

Aboav DA (1980) The arrangement of cells in a net. *Metallography* 13: 43–58

Alt S, Ganguly P & Salbreux G (2017) Vertex models: from cell mechanics to tissue morphogenesis. *Philosophical Transactions Royal Soc B Biological Sci* 372: 20150520

Anlaş AA & Nelson CM (2018) Tissue mechanics regulates form, function, and dysfunction. *Curr Opin Cell Biol* 54: 98–105

Aumailley M (2012) The laminin family. *Cell Adhes Migr* 7: 48–55

Ayad NME, Kaushik S & Weaver VM (2019) Tissue mechanics, an important regulator of development and disease. *Philosophical Transactions Royal Soc B* 374: 20180215

Balcioglu HE, Balasubramaniam L, Stirbat TV, Doss BL, Fardin M-A, Mège R-M & Ladoux B (2020) A subtle relationship between substrate stiffness and collective migration of cell clusters. *Soft Matter* 16: 1825–1839

Bhatia SK, Rashid A, Chrenek MA, Zhang Q, Bruce BB, Klein M, Boatright JH, Jiang Y, Grossniklaus HE & Nickerson JM (2016) Analysis of RPE morphometry in human eyes. *Mol Vis* 22: 898–916

Bi D, Lopez JH, Schwarz JM & Manning ML (2015) A density-independent rigidity transition in biological tissues. *Nat Phys* 11: 1074–1079

Bok D (1993) The retinal pigment epithelium: a versatile partner in vision. *J Cell Sci* 1993: 189–195

Chiu SN (1995) Aboav-Weaire's and Lewis' laws—A review. *Mater Charact* 34: 149–165

Chong NHV, Keonin J, Luthert PJ, Frennesson CI, Weingeist DM, Wolf RL, Mullins RF & Hageman GS (2005) Decreased Thickness and Integrity of the Macular Elastic Layer of Bruch's Membrane Correspond to the Distribution of Lesions Associated with Age-Related Macular Degeneration. *Am J Pathology* 166: 241–251

Claybon A & Bishop AJR (2011) Dissection of a Mouse Eye for a Whole Mount of the Retinal Pigment Epithelium. *J Vis Exp*

Di Russo J, Luik A, Yousif L, Budny S, Oberleithner H, Hofschröer V, Klingauf J, Bavel E, Bakker EN, Hellstrand P, *et al* (2016) Endothelial basement membrane laminin 511 is essential for shear stress response. *Embo J* 36: 183–201

Di Russo J, Young JL, Wegner JW, Steins T, Kessler H & Spatz JP (2021) Integrin **α**5**β**1 nano-presentation regulates collective keratinocyte migration independent of substrate rigidity. *Elife* 10: e69861

Eichinger JF, Haeusel LJ, Paukner D, Aydin RC, Humphrey JD & Cyron CJ (2021) Mechanical homeostasis in tissue equivalents: a review. *Biomech Model Mechan* 20: 833–850

561 Funaki M & Janmey PA (2017) Biology and Engineering of Stem Cell Niches. *Part Iii Des Smart*
562 *Biomaterials Mimic Control Stem Cell Niche*: 363–373

563 German O, Buzzi E, Rotstein N, Rodriguez-Boulan E & Politi L (2008) Retinal pigment epithelial cells
564 promote spatial reorganization and differentiation of retina photoreceptors. *J Neurosci Res* 86:
565 3503–3514

566 Hahn B-S & Labouesse M (2001) Tissue integrity: Hemidesmosomes and resistance to stress. *Curr*
567 *Biol* 11: R858–R861

568 Hannezo E, Prost J & Joanny J-F (2014) Theory of epithelial sheet morphology in three dimensions.
569 *Proc National Acad Sci* 111: 27–32

570 Humphrey JD, Dufresne ER & Schwartz MA (2014) Mechanotransduction and extracellular matrix
571 homeostasis. *Nat Rev Mol Cell Biology* 15: 802–12

572 Jaumouillé V, Cartagena-Rivera AX & Waterman CM (2019) Coupling of **β**2 integrins to actin by a
573 mechanosensitive molecular clutch drives complement receptor-mediated phagocytosis. *Nat Cell*
574 *Biol* 21: 1357–1369

575 Kaliman S, Hubert M, Wollnik C, Nuić L, Vurnek D, Gehrer S, Lovrić J, Dudziak D, Rehfeldt F & Smith
576 A-S (2021) Mechanical Regulation of Epithelial Tissue Homeostasis. *Phys Rev X* 11: 031029

577 Kaliman S, Jayachandran C, Rehfeldt F & Smith A-S (2016) Limits of Applicability of the Voronoi
578 Tessellation Determined by Centers of Cell Nuclei to Epithelium Morphology. *Front Physiol* 7:
579 551

580 Kim S, Cai M & Hilgenfeldt S (2014) Lewis' law revisited: the role of anisotropy in size–topology
581 correlations. *New J Phys* 16: 015024

582 Kim Y-K, Yu H, Summers VR, Donaldson KJ, Ferdous S, Shelton D, Zhang N, Chrenek MA, Jiang Y,
583 Grossniklaus HE, *et al* (2021) Morphometric Analysis of Retinal Pigment Epithelial Cells From
584 C57BL/6J Mice During Aging. *Invest Ophth Vis Sci* 62: 32

585 Kozyrina AN, Piskova T & Di Russo J (2020) Mechanobiology of Epithelia From the Perspective of
586 Extracellular Matrix Heterogeneity. *Frontiers Bioeng Biotechnology* 8: 596599

587 Kwon W & Freeman SA (2020) Phagocytosis by the Retinal Pigment Epithelium: Recognition,
588 Resolution, Recycling. *Front Immunol* 11: 604205

589 Lakkaraju A, Umapathy A, Tan LX, Daniele L, Philp NJ, Boesze-Battaglia K & Williams DS (2020) The
590 Cell Biology of the Retinal Pigment Epithelium. *Prog Retin Eye Res* 78: 100846

591 Lewis FT (1928) The correlation between cell division and the shapes and sizes of prismatic cells in
592 the epidermis of cucumis. *Anat Rec* 38: 341–376

593 Lewis FT (1931) A comparison between the mosaic of polygons in a film of artificial emulsion and the
594 pattern of simple epithelium in surface view (cucumber epidermis and human amnion). *Anat Rec*
595 50: 235–265

596 Malinverno C, Corallino S, Giavazzi F, Bergert M, Li Q, Leoni M, Disanza A, Frittoli E, Oldani A, a, *et*
597 *al* (2017) Endocytic reawakening of motility in jammed epithelia. *Nat Mater* 16: 587

598 Mongera A, ro, Rowghanian P, Gustafson HJ, Shelton E, Kealhofer DA, Carn EK, Serwane F, Lucio
599 AA, Giammona J, *et al* (2018) A fluid-to-solid jamming transition underlies vertebrate body axis
600 elongation. *Nature*

601 Müller C, Charniga C, Temple S & Finnemann SC (2018) Quantified F-Actin Morphology Is Predictive
602 of Phagocytic Capacity of Stem Cell-Derived Retinal Pigment Epithelium. *Stem Cell Rep* 10:
603 1075–1087

604 Newsome DA, Huh W & Green WR (1987) Bruch's membrane age-related changes vary by region.
605 *Curr Eye Res* 6: 1211–1221

606 Nobeschi L, Freymuller E & Smith RL (2006) Intercellular Junctions in Rabbit Eye Ora Serrata.
607 *Anatomia Histologia Embryologia* 35: 287–292

608 Oria R, Wiegand T, Escribano J, Elosegui-Artola A, Uriarte JJ, Moreno-Pulido C, Platzman I,
609 Delcanale P, Albertazzi L, Navajas D, *et al* (2017) Force loading explains spatial sensing of ligands
610 by cells. *Nature* 552: 219–224

611 Palamidessi A, Malinverno C, Frittoli E, Corallino S, Barbieri E, Sigismund S, Beznoussenko GV,
612 Martini E, Garre M, Ferrara I, *et al* (2019) Unjamming overcomes kinetic and proliferation arrest in
613 terminally differentiated cells and promotes collective motility of carcinoma. *Nat Mater* 18: 1252–
614 1263

615 Parinot C, Rieu Q, Chatagnon J, Finnemann SC & Nandrot EF (2014) Large-Scale Purification of
616 Porcine or Bovine Photoreceptor Outer Segments for Phagocytosis Assays on Retinal Pigment
617 Epithelial Cells. *J Vis Exp*

618 Park J-AA, Kim JH, Bi D, Mitchel JA, Qazvini NT, Tantisira K, Park CY, McGill M, Kim S-HH, Gweon B,
619 *et al* (2015) Unjamming and cell shape in the asthmatic airway~epithelium. *Nat Mater* 14: 1040–8

620 Pérez-González C, Ceada G, Greco F, Matejčić M, Gómez-González M, Castro N, Menendez A, Kale
621 S, Krndija D, Clark AG, *et al* (2021) Mechanical compartmentalization of the intestinal organoid
622 enables crypt folding and collective cell migration. *Nat Cell Biol*: 1–13

623 Przybyla L, Lakins JN, Sunyer R, Trepat X & Weaver VM (2016) Monitoring developmental force
624 distributions in reconstituted embryonic epithelia. *Methods* 94: 101–113

625 Raymond SM & Jackson IJ (1995) The retinal pigmented epithelium is required for development and
626 maintenance of the mouse neural retina. *Curr Biol* 5: 1286–1295

627 Rivier N (2006) Statistical crystallography Structure of random cellular networks. *Philosophical Mag*
628 *Part B* 52: 795–819

629 Schiller HB, Hermann M-R, Polleux J, Vignaud T, Zanivan S, Friedel CC, Sun Z, Raducanu A,
630 Gottschalk K-E, Théry M, *et al* (2013) **β**1- and **α**v-class integrins cooperate to regulate myosin II
631 during rigidity sensing of fibronectin-based microenvironments. *Nat Cell Biol* 15: 625–636

632 Song J, Zhang X, Buscher K, Wang Y, Wang H, Di Russo J, Li L, Lutke-Enking S, Zarbock A, er, *et al*
633 (2017) Endothelial Basement Membrane Laminin 511 Contributes to Endothelial Junctional
634 Tightness and Thereby Inhibits Leukocyte Transmigration. *Cell Reports* 18: 1256–1269

635 Song MJ, Quinn R, Nguyen E, Hampton C, Sharma R, Park TS, Koster C, Voss T, Tristan C, Weber C,
636 *et al* (2023) Bioprinted 3D outer retina barrier uncovers RPE-dependent choroidal phenotype in
637 advanced macular degeneration. *Nat Methods* 20: 149–161

638 Strauss O (2005) The Retinal Pigment Epithelium in Visual Function. *Physiol Rev* 85: 845–881

639 Stringer C, Wang T, Michaelos M & Pachitariu M (2021) Cellpose: a generalist algorithm for cellular
640 segmentation. *Nat Methods* 18: 100–106

641 Todorović V, Kligys KR, Dusek RL, Jones JCR & Green KJ (2013) Encyclopedia of Biological
642 Chemistry (Second Edition). *Cell Archit Funct Article Titles D*: 636–643

643 Vishwakarma M, Di Russo J, Probst D, Schwarz US, Das T & Spatz JP (2018) Mechanical interactions
644 among followers determine the emergence of leaders in migrating epithelial cell collectives. *Nat*
645 *Commun* 9: 3469

646 Volland S, Esteve-Rudd J, Hoo J, Yee C & Williams DS (2015) A Comparison of Some Organizational
647 Characteristics of the Mouse Central Retina and the Human Macula. *Plos One* 10: e0125631

648 Wald G & Brown PK (1956) Synthesis and Bleaching of Rhodopsin. *Nature* 177: 174–176

649 Weaire D (1974) Some remarks on the arrangement of grains in a polycrystal. *Metallography* 7: 157–
650 160

651 Young RW & Bok D (1969) Partecipation of the Retinal Pigment Epithelium in the Rod Outer
652 Segment Renewal Process. *J Cell Biology* 42: 392–403

653

654

SUPPLEMENTARY INFORMATION

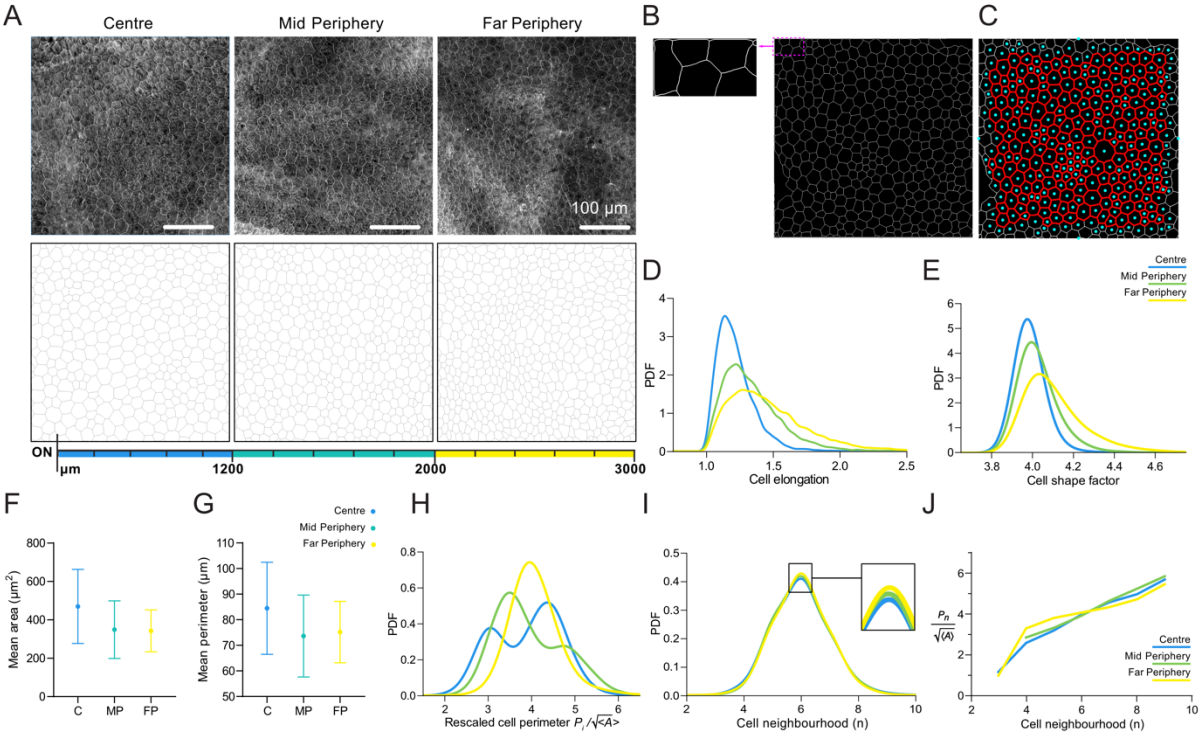

Supplementary Figure 1: ***(A)*** *representative confocal images of murine RPE stained for F-actin (top row) and post-processed segmented skeletons used for the morphometric characterisation (bottom row).* ***(B)*** *Representative cellpose segmentation artefact at the image edge and* ***(C)*** *resulting cells (blue) and neighbourhood (red) considered in the analyses. Probability density function (PDF) of cell elongation* ***(D)*** *and cell shape factor for the different retinal regions.* ***(F, G)*** *Mean and standard deviation of the mean cellular area and perimeter respectively.* ***(H)*** *PDF of the rescaled cell perimeters defined as* $P_i/\sqrt{A}$*,* P_i *being the individual cell perimeter. Topological characteristics of the RPE monolayer such as PDF of cell neighbourhood* ***(I)*** *and Desh's law representing the relationship between cellular perimeter and shape varying for three different regions. All data were collected from at least 3 mice.*

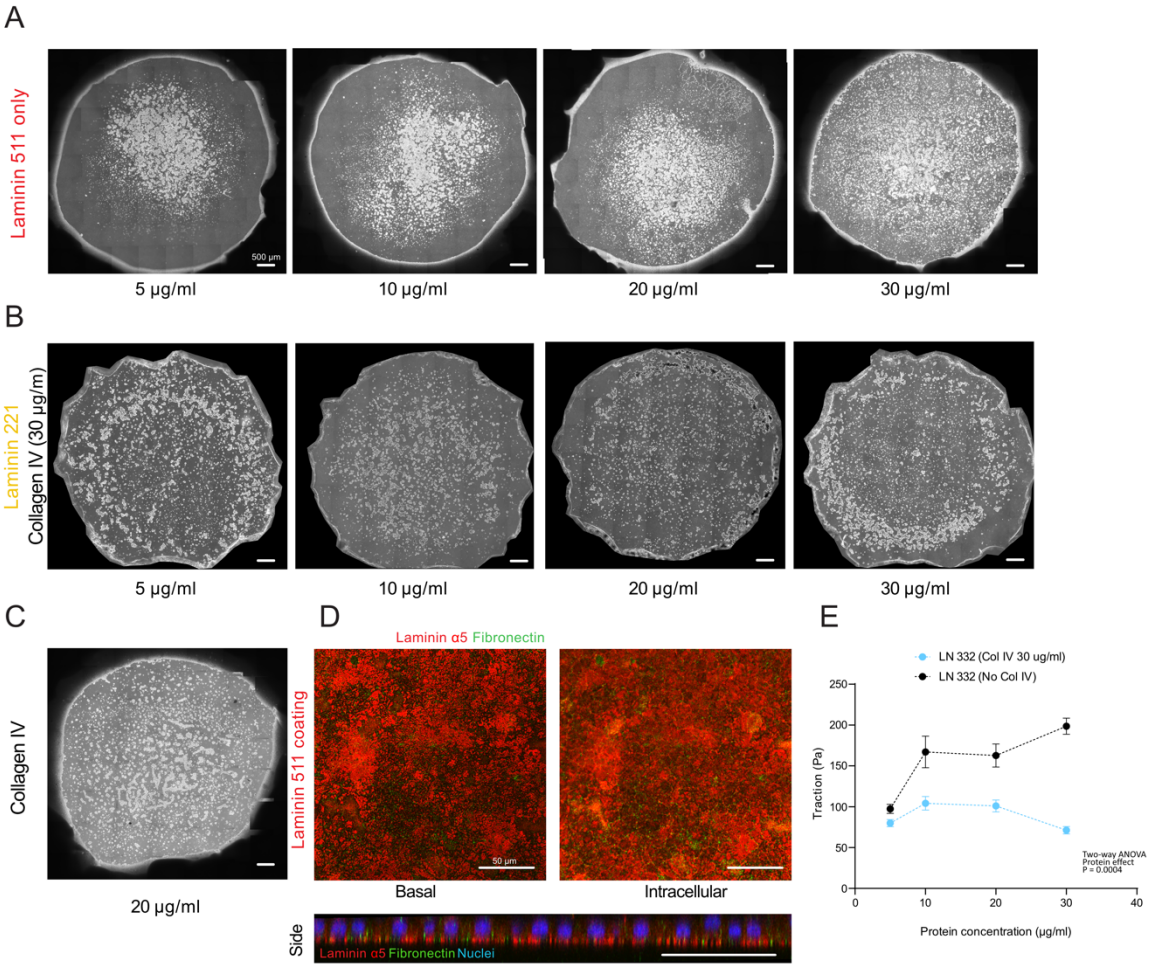

Supplementary figure 2: Protein composition of polyacrylamide gel surface coating is crucial for cell adhesion strength. *Representative overview images of colonies hiPSC-RPE cells seeded on 4 kPa gels coated with different concentrations of laminin 511* ***(A)****, laminin 221 combined with collagen type IV (30 µg/ml)* ***(B)*** *and pure collagen type IV (20 µg/ml)* ***(C)*** *indicating the insufficient cellular adhesion and monolayer formation in these experimental conditions. Scale bar 500 µm.* ***(D)*** *Immunofluorescent images of the laminin 511 coated gel surface stained for ECM proteins show the absence of fibronectin protein deposition after one week in culture. Top row represents the signal from laminin α5 (red) and fibronectin (green) at the basal surface and within the monolayer. Fibronectin signal appears to be intracellular as shown in the side view of the monolayer.* ***(E)*** *The presence of collagen type IV in the laminin 332 containing coating solution decreases the traction forces exerted by cells. This difference becomes less significant at lower laminin concentration. Data are shown as mean ± SEM. ***p=0.0004 for the protein effect using mixed-effects model (REML) with the Geisser-Greenhouse correction.*

657

658

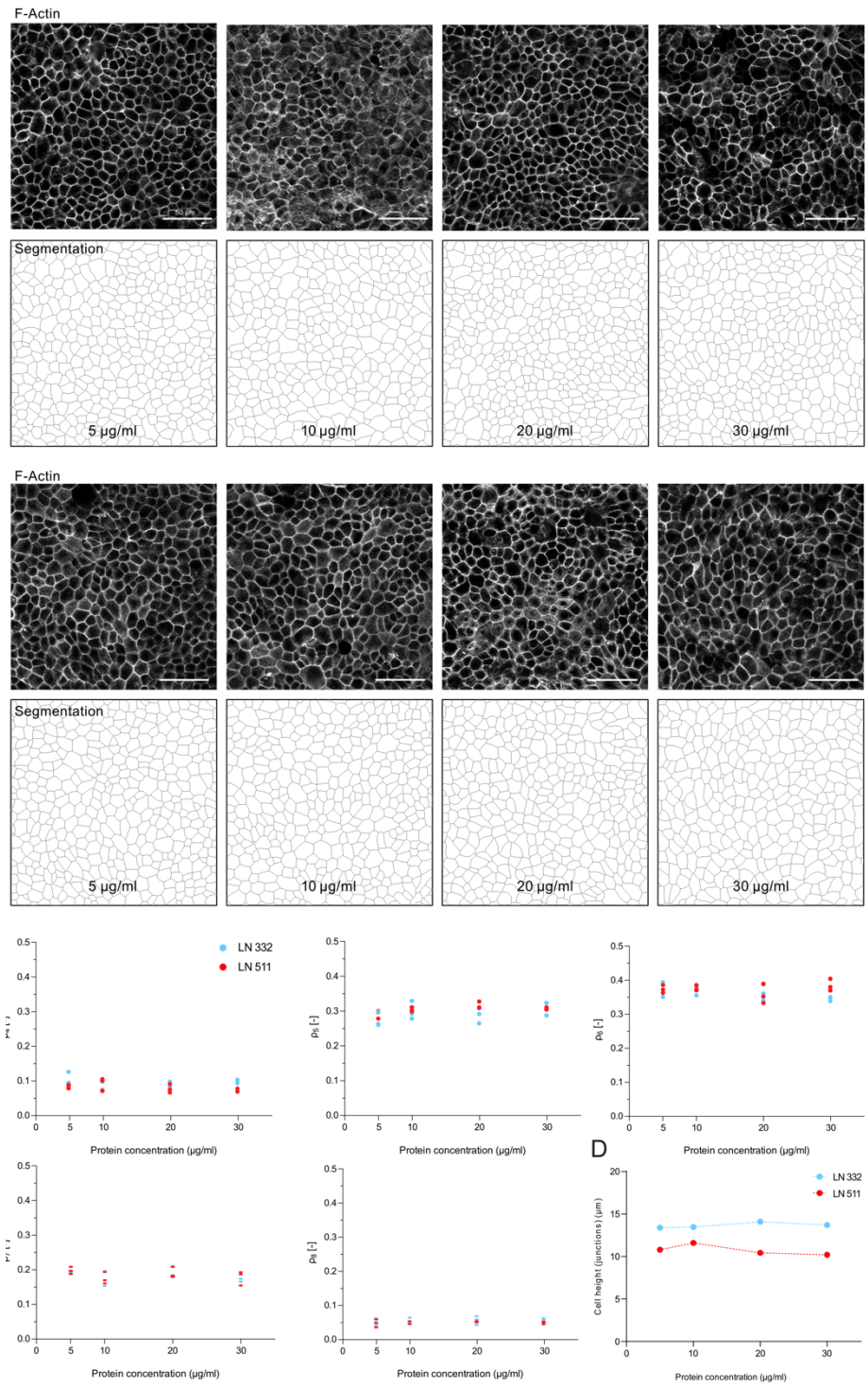

Supplementary figure 3: Structure and topological stability of RPE in vitro. *Representative confocal images of one-week cultured hiPSC-RPE monolayers on 4 kPa PAA gels coated with different concentrations of laminin 511* ***(A)*** *or laminin 332* ***(B)*** *both in presence of collagen type IV (30 µg/ml). The top row represents the actin cytoskeleton network in the stained samples and the bottom row shows segmented images used for morphometric analysis.* ***(C)*** *Probabilities of the cellular neighbourhood (ρ_n) from 4 (ρ_4) "squares" to 8 (ρ_8) "octagon" indicating the stable neighbourhood environment regardless of the protein surface concentration. Data are from 3 independent experiments with 3 independent fields of view in each experiment.*

660 *Table 1: List of antibodies used in this work*

Name	Origin	Source	Concentration (µg/ml) / Dilution
Anti mouse laminin 111 (pan-Laminin)	rabbit	Gift from Lydia Sorokin	Rabbit serum, 1:2000
Anti mouse laminin **α**1 (clone 200)	rat	Gift from Lydia Sorokin	Hybridoma supernatant
Anti mouse laminin **α**2 (clone 4H8-2)	rat	Gift from Lydia Sorokin	Hybridoma supernatant
Anti human laminin 332	rabbit	Gift from Monique Aumailley	Rabbit serum, 1:2000
Anti mouse laminin **α**4	rabbit	Gift from Lydia Sorokin	Rabbit serum, 1:1000
Anti mouse laminin **α**5	rabbit	Gift from Lydia Sorokin	Rabbit serum, 1:1000
Anti mouse collagen type IV	mouse	Merck Millipore, AB756P	12.5
Anti mouse collagen type I	rabbit	Novusbio, NB600-408	5
Anti mouse elastin	rabbit	Abcam, ab21610	5
Phalloidin iFluor 647		Abcam, ab176753	1x
Phalloidin iFluor 488		Abcam, ab176759	1x
Ant human ZO1	rabbit	Thermo Fisher, 61-7300	5
Anti human ezrin (clone 3C12)	mouse	Abcam, ab4069	20
Anti human fibronectin	rabbit	Sigma, F3648	2.5
Secondary antibodies			
Anti-mouse-IgG AF488	goat	Invitrogen, A11001	4
Anti-mouse-IgG AF594	goat	Invitrogen, A11005	4
Anti-mouse-IgG AF647	goat	Jackson/Dianova, 111-605-144	10
Anti-rabbit-IgG AF594	goat	Invitrogen, A11012	4
Anti-rabbit-IgG AF647	goat	Molecular Probes, A21235	10
Anti-rat-IgG AF555	goat	Invitrogen, A21434	4
Anti-rat-IgG AF647	goat	Thermo Fisher, A21247	10

661
662

663 ***Table 2: Number of cells in vitro analysed for morphometric and topological parameters***

	Laminin 322			Laminin 511		
	Exp 1	Exp 2	Exp 3	Exp 1	Exp 2	Exp 3
5 µg/mL	440 (454)	638 (654)	715 (736)	606 (625)	686 (710)	727 (753)
10 µg/mL	479 (495)	697 (719)	654 (679)	547 (561)	575 (594)	396 (415)
20 µg/mL	627 (641)	683 (698)	608 (634)	559 (572)	831 (856)	480 (499)
30 µg/mL	529 (539)	325 (334)	637 (660)	513 (525)	710 (737)	759 (782)

664

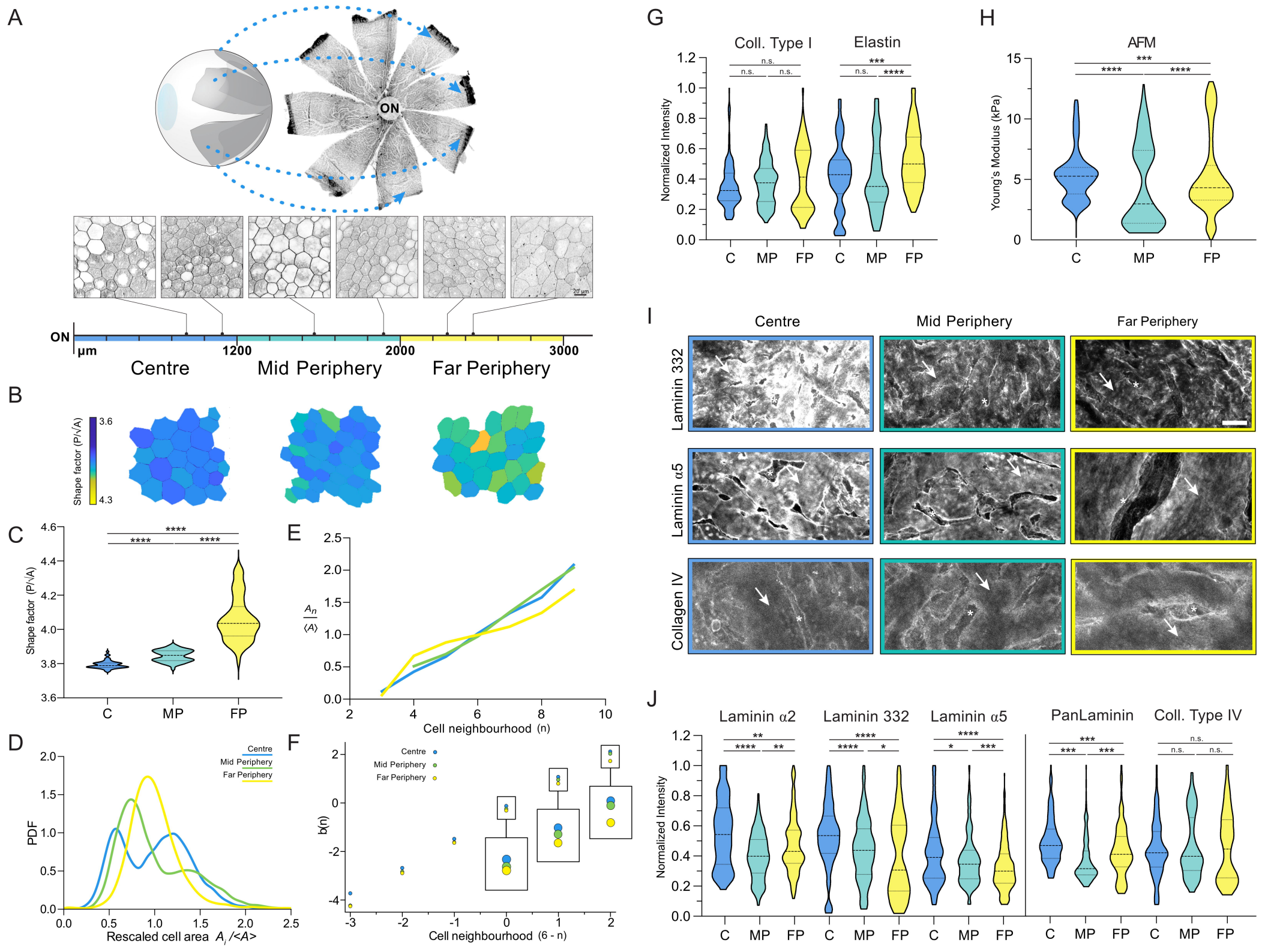
A
ON
20 µm
ON
µm
1200
2000
3000
Centre
Mid Periphery
Far Periphery
B
Shape factor (P/√A)
3.6
4.3
C
Shape factor (P/√A)
C
MP
FP
D
PDF
Rescaled cell area $A_i/\langle A\rangle$
Centre
Mid Periphery
Far Periphery
E
$\frac{A_n}{\langle A\rangle}$
Cell neighbourhood (n)
F
b(n)
Cell neighbourhood (6 - n)
Centre
Mid Periphery
Far Periphery
G
Coll. Type I
Elastin
Normalized Intensity
n.s.
***
****
H
AFM
Young's Modulus (kPa)
I
Centre
Mid Periphery
Far Periphery
Laminin 332
Laminin α5
Collagen IV
J
Laminin α2
Laminin 332
Laminin α5
PanLaminin
Coll. Type IV
Normalized Intensity

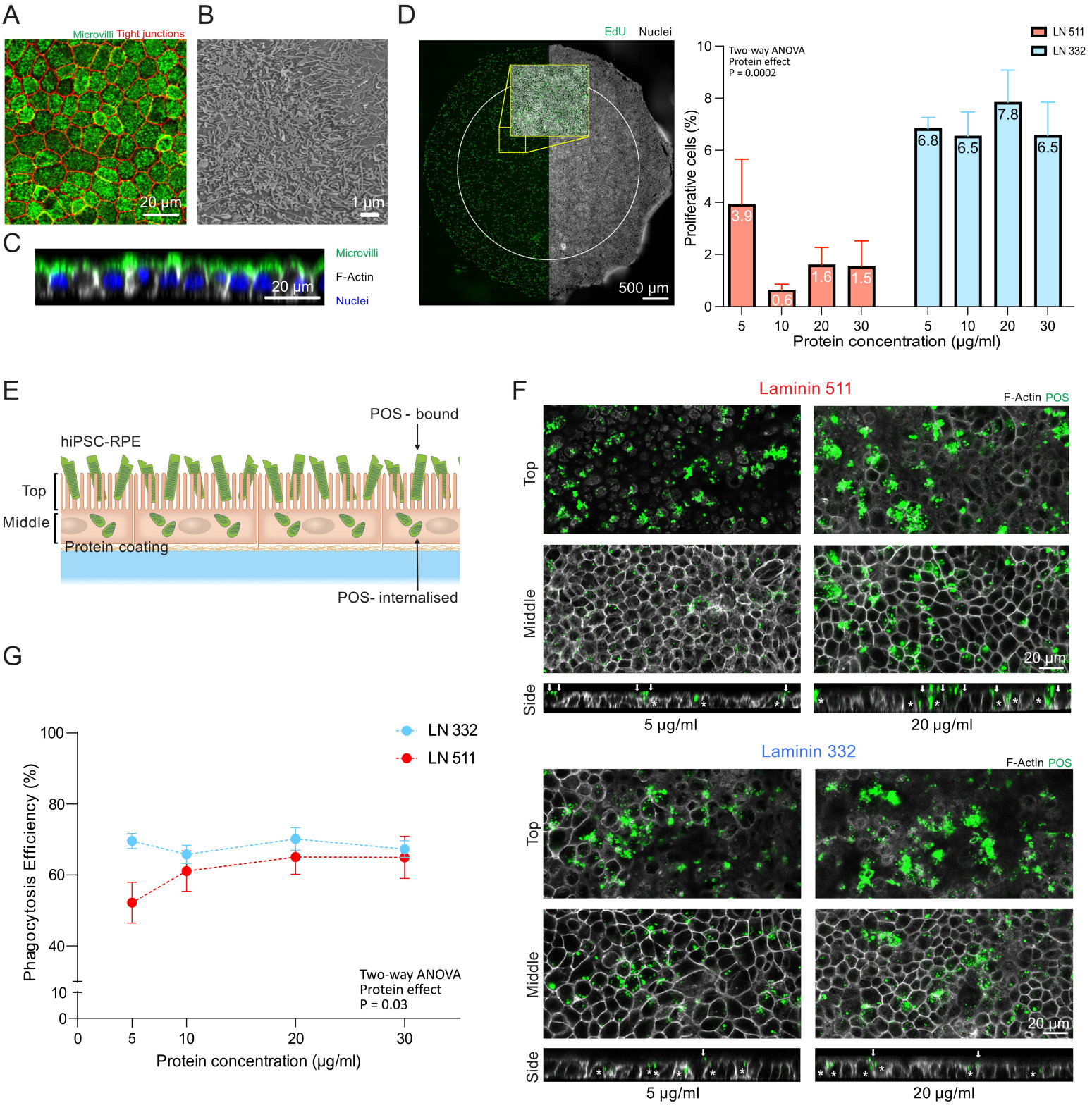
A
Microvilli Tight junctions
20 µm
B
1 µm
C
Microvilli
F-Actin
Nuclei
20 µm
D
EdU Nuclei
500 µm
LN 511
LN 332
Two-way ANOVA
Protein effect
P = 0.0002
Proliferative cells (%)
3.9
0.6
1.6
1.5
6.8
6.5
7.8
6.5
Protein concentration (µg/ml)
E
POS - bound
hiPSC-RPE
Top
Middle
Protein coating
POS- internalised
F
Laminin 511
F-Actin POS
Top
Middle
Side
20 µm
5 µg/ml
20 µg/ml
Laminin 332
F-Actin POS
Top
Middle
Side
20 µm
5 µg/ml
20 µg/ml
G
LN 332
LN 511
Phagocytosis Efficiency (%)
Two-way ANOVA
Protein effect
P = 0.03
Protein concentration (µg/ml)

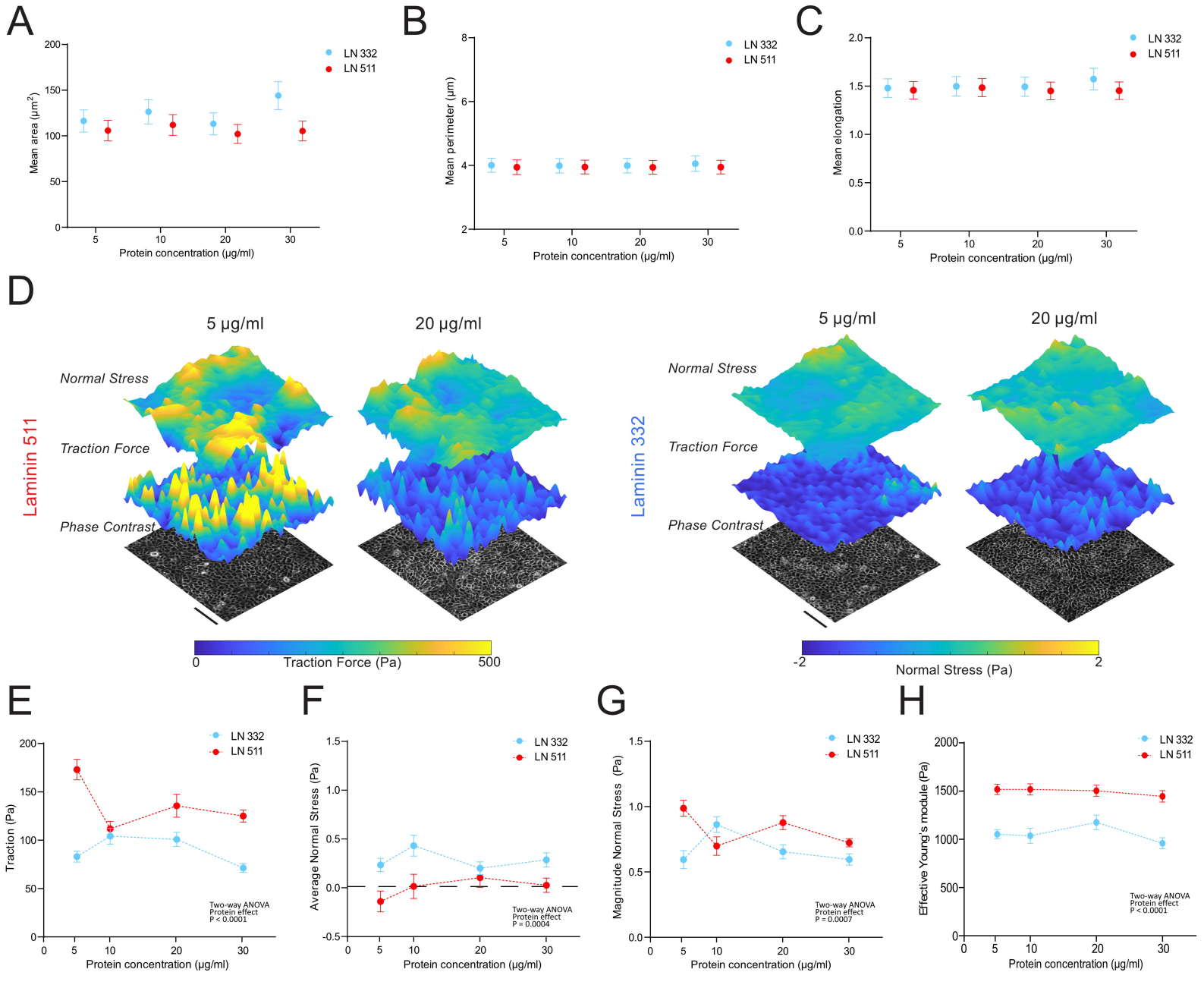
A
Mean area (μm²)
Protein concentration (μg/ml)
LN 332
LN 511
B
Mean perimeter (μm)
Protein concentration (μg/ml)
LN 332
LN 511
C
Mean elongation
Protein concentration (μg/ml)
LN 332
LN 511
D
5 μg/ml
20 μg/ml
Normal Stress
Traction Force
Phase Contrast
Laminin 511
Laminin 332
Traction Force (Pa)
Normal Stress (Pa)
E
Traction (Pa)
Protein concentration (μg/ml)
Two-way ANOVA
Protein effect
P < 0.0001
F
Average Normal Stress (Pa)
Protein concentration (μg/ml)
Two-way ANOVA
Protein effect
P = 0.0004
G
Magnitude Normal Stress (Pa)
Protein concentration (μg/ml)
Two-way ANOVA
Protein effect
P = 0.0007
H
Effective Young's module (Pa)
Protein concentration (μg/ml)
Two-way ANOVA
Protein effect
P < 0.0001

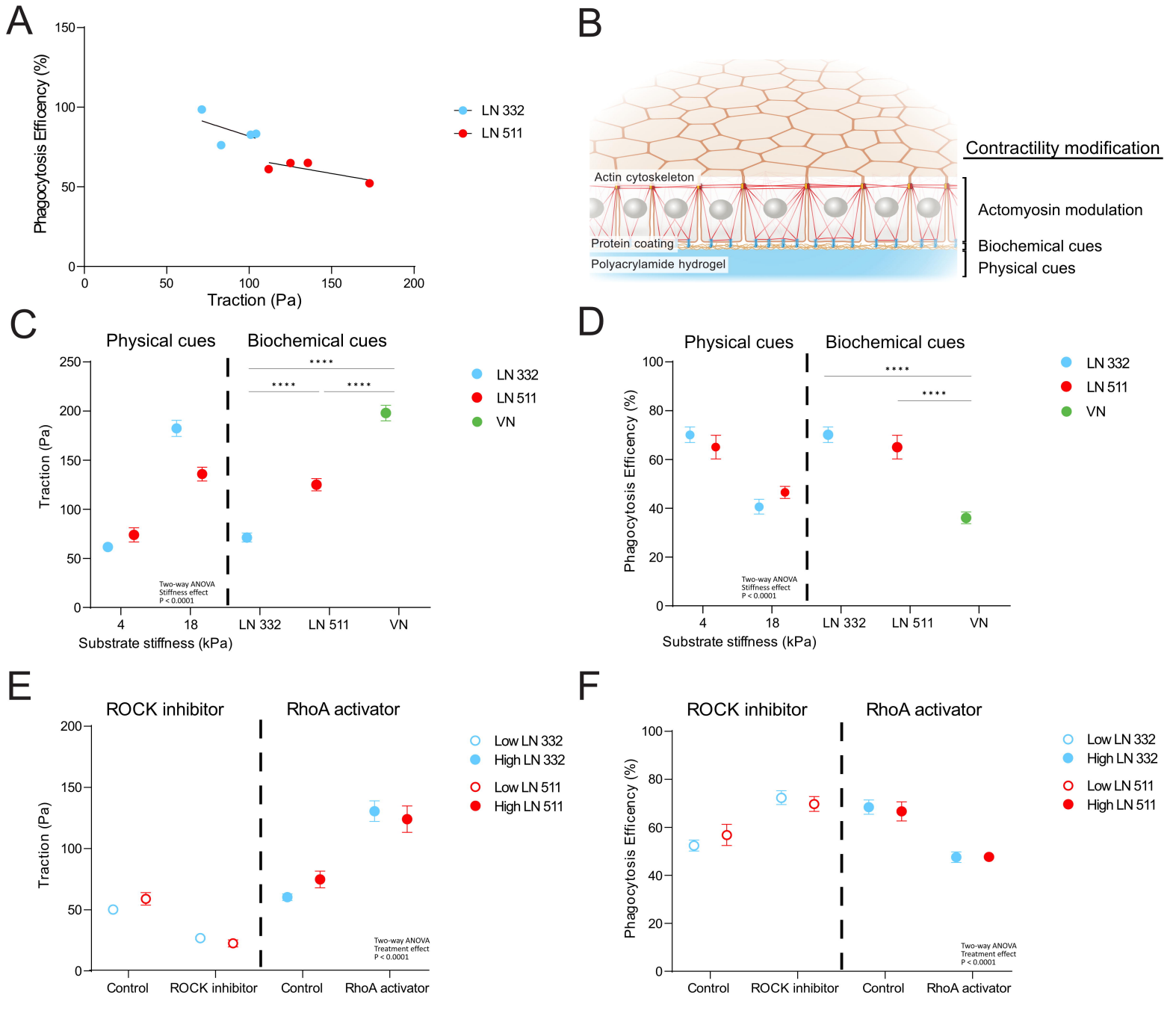
A
Phagocytosis Efficency (%)
Traction (Pa)
LN 332
LN 511
B
Contractility modification
Actin cytoskeleton
Actomyosin modulation
Protein coating
Biochemical cues
Polyacrylamide hydrogel
Physical cues
C
Physical cues
Biochemical cues
Traction (Pa)
Substrate stiffness (kPa)
Two-way ANOVA
Stiffness effect
P < 0.0001
LN 332
LN 511
VN
D
Physical cues
Biochemical cues
Phagocytosis Efficency (%)
Substrate stiffness (kPa)
Two-way ANOVA
Stiffness effect
P < 0.0001
LN 332
LN 511
VN
E
ROCK inhibitor
RhoA activator
Traction (Pa)
Control
ROCK inhibitor
Control
RhoA activator
Two-way ANOVA
Treatment effect
P < 0.0001
Low LN 332
High LN 332
Low LN 511
High LN 511
F
ROCK inhibitor
RhoA activator
Phagocytosis Efficency (%)
Control
ROCK inhibitor
Control
RhoA activator
Two-way ANOVA
Treatment effect
P < 0.0001
Low LN 332
High LN 332
Low LN 511
High LN 511